Green Chemistry

TUTORIAL REVIEW

View Article Online
View Journal

Cite this: DOI: 10.1039/d4gc05346j

Laser-induced carbonization technology towards biomass-derived carbon materials: mechanism, preparation and application

Xingjie Xu,[a] Mengdi Zhang,*[a] Chao Qi,[b] Yi Sun,[a] Lijun Yang,[c] Xin Gu,[a] Yanpeng Li,*[a] Mingbo Wu,[a] Bin Wang*[a] and Han Hu[a]

Received 24th October 2024,
Accepted 19th December 2024

DOI: 10.1039/d4gc05346j

rsc.li/greenchem

Biomass is considered as a desirable carbon source due to its abundance, low cost, environmental friendliness and sustainability. The traditional preparation methods of biomass-derived carbon materials, typically in-furnace pyrolysis, involve tedious and energy-consuming processes and require harsh operation conditions. In contrast, laser-induced carbonization is a facile, environmentally friendly and high-efficiency technique that can create an instantaneous thermal shock process for the rapid conversion of biomass into carbon, enabling it to more easily possess unique active sites that play powerful roles in energy storage and conversion applications. Besides, the microstructure and composition of laser-induced biomass-derived carbon materials (LIBCs) can be precisely regulated by adjusting precursor types and laser processing parameters. In this review, the current developments on LIBCs are elaborated. The laser-induced carbonization mechanism is first introduced, and the effects of laser parameters including laser power, scanning speed, laser spot defocus, and atmosphere on the carbonization process are discussed. A special focus is put on the functionalization treatment of LIBCs, including the doping of heteroatoms as well as the incorporation of metals or metal compounds. The applications of LIBCs in the fields of micro-supercapacitors, batteries, electrocatalysis, sensors, and so on are highlighted. Finally, the current challenges and future prospects of LIBCs are discussed.

Green foundation

1. The laser-induced carbonization technology has opened new avenues for producing biomass-derived carbon materials through greener, more sustainable methods. This approach minimizes energy consumption and eliminates the need for harmful chemicals. Its cost-effectiveness and adaptability have shown the potential to surpass traditional carbonization methods in specific applications.
2. If the scientific community and industry can establish scalable and cost-effective production routes for laser-induced biomass-derived carbon, they have the potential to lead the transition to sustainable material production, while unlocking significant economic and technological opportunities in the long term.
3. Growing global attention to sustainability makes the development of cost-competitive carbonization processes particularly critical. This review offers a comprehensive understanding of the mechanisms and applications of laser-induced carbonation technology, serving as a guide for optimizing green synthesis routes. By fostering innovation in sustainable material production, it will contribute to shaping the next generation of green chemistry practices.

Introduction

Carbon materials have played important roles in the advancement of human civilization. By virtue of their excellent electrical conductivity, thermal and mechanical properties, chemical stability, high specific surface area, as well as highly developed and tunable porosity, carbon materials have been widely used in a variety of fields, including sensing, catalysis, environmental governance, energy storage, biomedicine, and so on.[1–6]

[a]State Key Laboratory of Heavy Oil Processing, Advanced Chemical Engineering and Energy Materials Research Center, College of Chemistry and Chemical Engineering, Institute of New Energy, China University of Petroleum (East China), Qingdao 266580, China. E-mail: mdzhang@upc.edu.cn, liyanpeng@upc.edu.cn, bin.wang@upc.edu.cn
[b]Department of Sport Medicine, The Affiliated Hospital of Qingdao University, Qingdao 266300, China
[c]Qingdao Guanbaolin Activated Carbon Co. Ltd, Qingdao 266313, China

The selection of carbon precursors and processing methods is critical for the preparation of carbon materials with specific characteristics and functions. During the selection of ideal carbon precursors, multiple factors need to be taken into account, such as cost, property, source sustainability, and processing feasibility. As a renewable resource, biomass is generally categorized into plant biomass resources and animal biomass resources. Plant biomass mainly includes leaves, branches, fruits, and other organisms, the main components of which are cellulose, hemicellulose, and lignin. Animal biomass generally consists of shells, hides, and bones.[7,8] Approximately 140 billion tons of waste biomass are produced globally every year,[9] and they are typically treated by burning, which can cause serious environmental pollution. The development of biomass-derived carbon materials is a green and highly value-added utilization route of biomass. Compared with coal/petroleum-based carbon sources, biomass has the advantages of easy availability, abundant reserves, rapid regeneration, and environmental friendliness. In addition, most biomass materials possess abundant pores and heterogeneous elements (such as O, N, P, S, *etc.*).[10–12] The porous structure can be inherited and heteroatoms can be *in situ* doped into the carbon matrix after carbonization. The unique microstructure and properties of biomass-derived carbon materials are highly favorable in many application fields.[13] However, unlike high-purity carbon precursors, biomass usually contains unwanted elements, impurities, and contaminants, which adversely affect the quality of final carbon products. Therefore, biomass needs to be pre-treated with acidic or alkaline reagents before carbonization.

The diverse demands for the structures and properties of biomass-derived carbon materials have stimulated the development of various preparation methods. Common carbonization methods include in-furnace pyrolysis, hydrothermal carbonization, and microwave-assisted carbonization. In-furnace pyrolysis primarily involves the thermochemical decomposition of biomass at a high temperature (≥400 °C) under an inert atmosphere,[14] and the structure and composition of carbon materials can be controlled by adjusting the heating temperature, time, rate, and atmosphere, even by introducing templates or activation agents.[15,16] However, the preparation process is always highly energy-/time-consuming and environmentally harmful. Hydrothermal carbonization is a typical thermochemical transformation process in a closed system at a relatively low temperature (100–300 °C) and a self-generating pressure above 1 atm.[17] Although a more facile manipulation condition is applied, the obtained carbon usually has a low electrical conductivity and undeveloped pore structure, largely limiting its application scope. In the case of microwave-assisted carbonization, the biomass raw materials can be rapidly heated in a short period of time (5–30 min), resulting in a temperature gradient (500–1000 °C) from the inside to the outside.[18] The obtained biomass-derived carbon materials are characterized by high porosity and good electrical conductivity. However, it is difficult to control the heating rate under microwave irradiation, leading to low reproducibility and poor carbon quality.[19]

Laser-induced carbonization, as an emerging processing technology, has drawn enormous attention and holds great promise in the field of materials science. The photothermal effect induced by laser irradiation gives rise to the instantaneous heating and fast cooling of the target materials, contributing to an extremely high-temperature and high-pressure carbonization environment.[20] As a result, laser-induced carbon materials will exhibit unique structures and properties that are difficult to achieve by other carbonization methods.[21] Also, the carbonization process is straightforward, controllable, high-efficiency, and low-cost.[22] Another unparalleled advantage of laser-induced carbonization is to design fine carbon patterns on scales of different orders of magnitude from nanometers to millimeters on the substrate surface, making it ideally suitable for the fabrication of flexible and microelectronic devices.[23] In addition, computer-controlled laser systems are compatible with other material processing technologies such as roll-to-roll manufacturing,[24] painting,[25] and 3D printing.[26] In Table 1, the advantages and disadvantages of the various carbonization techniques are summarized. A remarkable work on laser-induced carbonization was reported by Tour's group in 2014. They used laser direct-writing technology to carbonize the surface of commercial polyimide (PI) film in air, and the resulting carbon was termed "laser-induced graphene (LIG)".[27] This innovative, one-step, and highly scalable process effectively converted sp^3-carbon to sp^2-carbon, producing highly conductive LIG materials that could be easily patterned into

Table 1 Advantages and disadvantages of carbonization methods[36–38]

Carbonization method	Advantages	Disadvantages
Laser-induced carbonization	1. Efficient and rapid conversion (nanoseconds-seconds) 2. Low energy consumption 3. High controllability 4. Precise patternability 5. High conductivity and flexibility	1. High equipment investment 2. Limited to surface processing 3. Poor homogeneity
In-furnace carbonization	1. Mature technique 2. High suitability for mass production 3. Low equipment investment 4. High adaptability	1. Time consuming (several hours) 2. High energy consumption 3. Complicated structure regulation process
Hydrothermal carbonization	1. Easy operation 2. Moderate operating conditions 3. Low equipment investment	1. Time consuming (several hours) 2. Low degree of carbonization 3. Difficult to process continuously 4. Poor conductivity
Microwave carbonization	1. Rapid conversion (several minutes) 2. Low energy consumption 3. Low equipment investment	1. Difficult temperature control 2. Low reproducibility 3. Poor homogeneity

electrodes for electrochemical energy storage devices. Over the past decade, the scope of precursor materials applicable to laser processing has been expanded to other polymers (such as polysulfone, polyethersulfone, polystyrene, and phenolic resin),[28] coal,[29] and natural biomass.[30] For example, three-dimensional porous graphene was successfully prepared by laser irradiation on pine wood in an Ar or H_2 atmosphere and showed excellent electrical conductivity and a high specific surface area, endowing it with great application potential in overall water splitting and supercapacitors.[31] It is apparent that laser-induced carbonization is an effective method to synthesize biomass-derived carbon materials, which not only allows for marvelous material properties, but also provides high flexibility in terms of material designability and functionality. Although there have been some reviews on laser-induced carbon materials, especially LIG,[32–34] the comprehensive discussion specific to laser-induced biomass-derived carbon (LIBCs) is still lacking.

Life cycle analysis (LCA) is a powerful means of evaluating the environmental impacts and economic benefits of conventional in-furnace pyrolysis and laser-induced carbonization. Due to the limited availability of LCA data for laser-induced carbonization, we are only able to provide a comparative discussion here. Regarding environmental impacts, the primary environmental burdens of in-furnace pyrolysis include emissions of CO_2, CO, and other waste gases, with a carbon footprint of 0.75–3 kg CO_2-eq. per kilogram of carbon produced.[35] Additionally, the release of volatile organic compounds (VOCs) may further impact air quality, and liquid residues such as tar could pose risks to water and soil systems.[39] In contrast, laser-induced carbonization is efficient and generates significantly less emissions. The carbon footprint during the production of each kilogram of carbon is approximately 0.3–1.1 kg CO_2-eq., with minimal generation of liquid residues, resulting in a relatively smaller ecological impact.[40] In terms of production cost, in-furnace pyrolysis, as an indirect heating technique by means of heating of resistance wire, suffers from high energy consumption and low efficiency. Also, multiple heat-resistant components, inert gas lines, and highly specialized manpower are required. As a result, most carbon materials synthesized by in-furnace pyrolysis remain expensive. In contrast, the laser acts directly on the surface of the precursor to induce its carbonization based on the photothermal effect, which is an energy-saving and efficient process.[27] Moreover, carbon materials with unique characteristics, such as a flexible all-in-one structure and 3D hierarchical structure, can be produced simply by laser processing and be applicable for a variety of microscale devices.[41] Such a quick, facile, yet effective technology greatly reduces the production costs of carbon materials.

In this review, we focus on the laser-induced controllable fabrication of carbon materials from biomass and their application in the fields of energy storage/conversion, sensors, and so on. As illustrated in Fig. 1, the mechanism and processing parameters of laser-induced carbonization are first introduced. Then, we summarize some representative works on the functionalized preparation of LIBCs and highlight their application progress in supercapacitors, batteries, electrocatalysis, sensors, and so on. Finally, the current challenges and the development prospects of LIBCs are also discussed.

Overview of laser-induced carbonization technology

The mechanism of laser-induced carbonization

Despite the straightforward operation of the laser-induced carbonization technology, the underlying material transformation

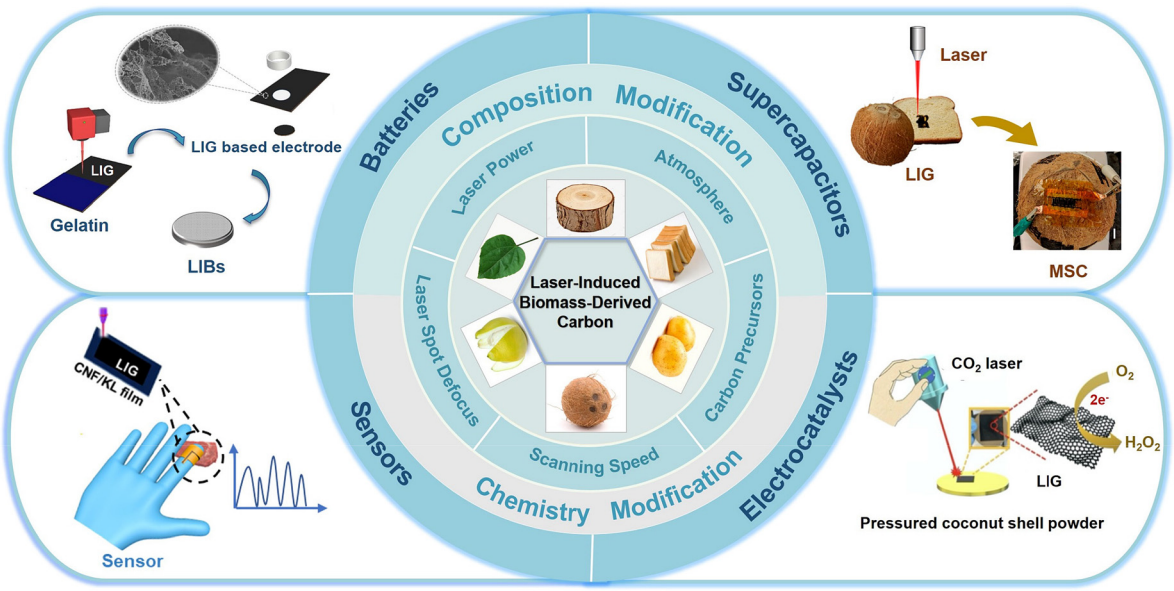

Fig. 1 An overview of the preparation, regulation and application of LIBCs.

process is extremely complex and the revelation of the carbonization mechanism is very challenging.[42] It is generally accepted that laser-induced carbonization is based on the photothermal effect. The laser can deposit a large amount of photothermal energy on the polymer substrate in a short period of time, resulting in a localized high temperature that breaks the C–O, C═O, and C–N bonds of the polymer.[43] Subsequently, some atoms are recombined to small molecules of gases, which do not have sufficient time to be fully released, thus creating a high-pressure reaction environment. Under such high temperature and pressure conditions, the remaining aromatic compounds are rearranged, and the sp^3 carbon atoms are transformed into sp^2 lattice carbons, resulting in the formation of LIG.[27]

In order to acquire more information on the laser-induced carbonization process, Dong *et al.* performed a molecular dynamics (MD) simulation with the ReaxFF potential in a nanosecond time scale. At a simulated pressure of ~3 GPa and temperature above 2400 K, PI was crystallized into layered graphene clusters. But at a lower pressure of 27 MPa, PI was decomposed into small molecules, demonstrating that high temperature and high pressure are indispensable for the formation of LIG.[44] Green *et al.* used ReaxFF reactive molecular dynamics to simulate the formation of LIG from five kinds of polymers, including polybenzimidazole, polyether (ether ketone), poly(ether imide), poly(polycarbonate), and poly (kapton) (Fig. 2a).[45] In this study, the temperature threshold of the LIG formation was determined by multiple simulations. The results revealed that a temperature below 2000 K led to the formation of amorphous structures, and a high temperature above 3500 K induced the complete decomposition of the polymer backbone with almost negligible LIG yield (Fig. 2b and c). The temperature range of 2500–3000 K was the optimal carbonization temperature, at which the quality and yield of LIG were the highest. The LIG showed an ordered graphite structure with 5-, 6-, and 7-membered rings, and the spacing between consecutive graphite sheets was 3.4–4.0 Å (Fig. 2d). In addition, the process of laser-induced graphitization is closely related to the structural characteristics of the repeating units in polymers, such as aromatic and imide units. Polymers with higher melting points and cross-linked thermoset plastics tend to exhibit high-quality conversion to LIG.[46] Based on the

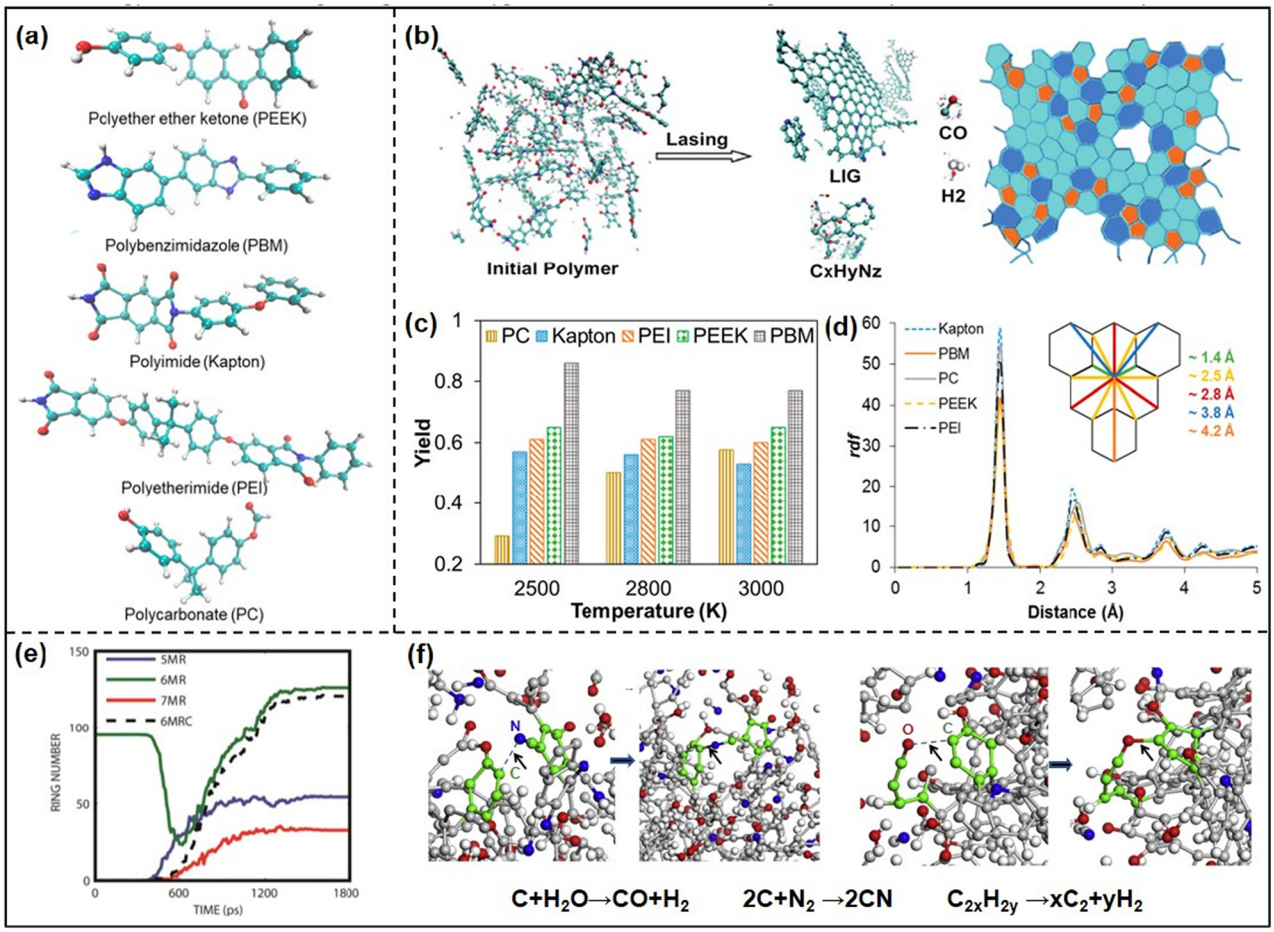

Fig. 2 (a) Molecular structure of the studied monomers; (b) schemes for lasing of polymers; (c) LIG yield at three different temperatures; (d) radial distribution function calculations for C–C atoms.[45] (e) Evolution of the carbon rings under 3000 K; (f) snapshots of t = 601.25 ps, 601.30 ps, 600.25 ps, and 600.30 ps (including relative paths).[44]

above research, Lin *et al.* employed MD simulation to track the atomic-scale dynamic evolution of PI molecules under laser irradiation (at a pressure of approximately 3 GPa and a temperature exceeding 2400 K), revealing the mechanisms of molecular bond cleavage and carbon network reorganization.[44] Initially (T = 2100 K), the 6-membered ring in PI underwent decomposition driven by high thermal energy, and the resulting nitrogen and oxygen radicals induced the bonding of the carbon rings. In this process, the main products were 5-membered rings and carbon dimers, and the heteroatoms were removed as CO, CN, H_2 or other by-products. As the temperature increased (*e.g.*, 2700 K), the 6-membered ring decomposed into 5-membered and the 7-membered rings to increase the crystallinity. Until higher temperatures (*e.g.*, 3000 K), the formation of 6-membered rings increases significantly, with the proportion of 6-membered rings rising from 58.8% at 2400 K to 95.6% at 3000 K. This change strongly contributed to the advancement of the transformation of sp^3 to sp^2 configuration of carbon (Fig. 2e and f). This study clearly illustrates the dynamic process from molecular bond cleavage to the formation of graphene, providing fundamental theoretical support for understanding structural rearrangement mechanisms in laser-induced carbonization.

The exploration of natural or biodegradable carbon precursors is essential to boost the development of "green" carbon-based devices.[47] However, the direct conversion of renewable natural biomass to carbon materials based on the laser-induced strategy is challenging, because polysaccharide chain biopolymers (such as cellulose) are prone to decomposing into volatile gases rather than forming carbon networks under the heat shock generated by laser irradiation.[46] The pretreatment of biomass and the optimization of laser processing techniques can solve this issue. Tour *et al.* found that cellulose molecules can be converted to aliphatic and aromatic carbon by laser irradiation under an inert atmosphere or in the presence of a flame retardant.[31] Later, Ye *et al.* also concluded that the main obstacle to the formation of LIG from biomass was that the components contained in biomass could easily be ablated or combusted into a variety of gases in air due to their flammability, thus the use of special flame-retardant treatments (such as a reducing/inert gas environment and flame-retardant agents) or multi-step laser treatments under low power was required, which undoubtedly increased the cost of preparation.[48] Considering that chitosan-based biomass had excellent flame-retardant properties, they succeeded in the conversion of chitosan derivatives (including carboxymethyl chitosan, chitosan oligosaccharides, and chitosan hydrochloride) into three-dimensional LIG by using a one-step laser treatment in air.[49] In addition, Strauss's group proposed that pre-carbonization was an essential condition for the direct laser-induced carbonization of biomass. The pre-carbonization process could effectively promote the condensation and cross-linking of biomass molecules and avoid molecule evaporation under high-energy laser irradiation.[50] A stable carbon network structure was formed by the pre-carbonization of citric acid and urea at 300 °C and provided a more stable substrate for the subsequent laser treatment, greatly improving the homogeneity and efficiency of laser-induced carbonization.[51]

The laser-induced formation of carbon materials involves multiple structural and chemical changes from the molecular to the nanoscale, and advanced *in situ* techniques will play a crucial role in resolving this dynamic transformation process. For example, *in situ* TEM enables real-time observation of the dynamic growth process of laser-induced carbon nanomaterials and provides insights into the role of catalysts for the regulation of the carbon structure. Through *in situ* TEM, it was found that the iron nanoparticles decomposed by laser irradiation of ferrocene moved randomly on the surface of the carbon film and changed their shapes continuously. These nanoparticles formed tube-like or onion-like carbon structures along their movement path (Fig. 3a). The particle surface alternated between spherical and crystalline states, with the graphitization process occurring preferentially during the stage of crystallization. The formation of these carbon nanomaterials was closely related to the crystallographic orientation of the particles.[52] *In situ* Raman spectroscopy combined with machine learning can be used to track the dynamic evolution of LIG. The evolution trends of D and G peaks were obtained by real-time acquisition of *in situ* Raman spectra and were analyzed using machine learning algorithms. At the early stage of laser irradiation, the carbon material showed a disordered state with a highly defective structure, and the D band signal was stronger. As laser irradiation continued, the accumulation of local heat facilitated the transition from sp^3 to sp^2. The

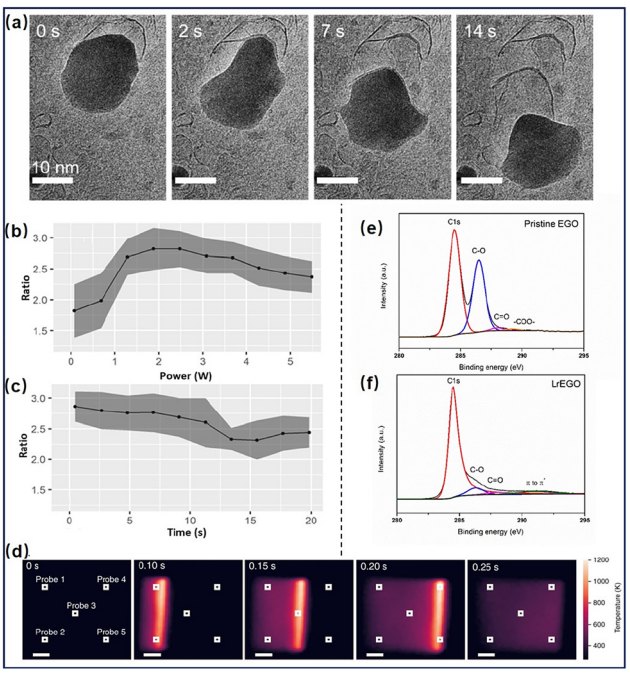

Fig. 3 (a) TEM images of nanoparticles' movement paths under a laser.[52] (b) Dependence plots of G/D ratio for power; (c) dependence plots of G/D ratio for time.[53] (d) The infrared images of EGO under a laser; (e) high resolution X-ray photoelectron spectroscopy (XPS) C 1s of pristine EGO; (f) high resolution XPS C 1s of LrEGO.[54]

optimal G/D ratio for the conversion from PI to LIG occurred at laser powers between 1.9 W and 2.5 W. However, at high power, the sp^2 structure was damaged, leading to a decrease in the G/D ratio (Fig. 3b and c).[53] Another study used *in situ* infrared thermal imaging to monitor the thermal evolution and reduction phenomena of electrochemical graphene oxide (EGO) films under a laser. When using a 1064 nm infrared laser, the surface temperature of the EGO film increased with the increase of laser energy density and the number of pulses, reaching a peak of 1692.2 K. This high temperature promoted the removal of oxygen-containing functional groups, such as carboxyl and carbonyl groups, and facilitated the graphitization of the carbon structure (Fig. 3d–f). Furthermore, it was observed in *in situ* infrared thermography that EGO could be uniformly reduced to LrEGO under multiple laser scans due to the accumulation of laser thermal energy.[54]

In short, due to the complex structure of biomass precursors as well as the unique carbonization environment and nanosecond reaction time induced by laser irradiation, it is very challenging to predict and monitor the interaction between the laser beam and the biomass, and the precise and in-depth conversion mechanism of LIBCs is still under debate.

Process parameters of laser-induced carbonization

The physical and chemical properties of laser-induced carbon materials depend not only on the properties of the raw material, but also to a large extent on the characteristics of the laser, the system setup, and the immediate environment for performing the processing. It has been demonstrated that the ratio of C, N, and O atoms and the surface wettability of LIG can be tuned by altering the laser power or laser scanning speed.[55–57] Khandelwal *et al.* changed the substrate composition by applying another layer of polyamide acid/H_3BO_3 on the LIG and then performing secondary laser carbonization to prepare N,B co-doped LIG.[58] Cai *et al.* demonstrated that the capacitive properties of LIG can be improved by changing the laser carbonization atmosphere from air to inert gas.[59] Considering the far-reaching significance of the laser processing technique in the structure and performance of carbon, the research progress in the regulation of laser parameters, including laser power, scanning speed, laser spot defocus, and atmosphere, is discussed in detail in this section.

Laser wavelength. As a pivotal parameter in the processing of LIBCs, laser wavelength variations across the ultraviolet (UV, 100–380 nm), visible (380–780 nm), and infrared (IR, 780 nm–50 μm) spectra directly influence the microstructure and surface chemical properties of the carbon materials.[6] Due to the shorter wavelengths and shallower penetration depths, UV lasers primarily focus on the surface of materials to form high-resolution structures with micrometer to nanometer porosity. Wang *et al.* demonstrated that using a 5 W UV laser with a wavelength of 355 nm on PI films produced LIG with surface pores of micro- and nanoscale dimensions.[60] In contrast, an IR laser has a longer wavelength and is able to penetrate deeper into the material, which is particularly effective for thicker substrates (*e.g.*, PI, GO, wood, and bread).[46] Under the irradiation of a CO_2 laser, these materials can be converted into LIG with distinct layered structures. Wang *et al.* also employed a CO_2 laser with a wavelength of 10.6 μm on PI films, resulting in LIG with microscale porosity and sheet-like features (Fig. 4a).[60] Moreover, compared with visible and IR lasers, UV lasers can induce stronger deoxygenation reactions, which can significantly reduce the oxygen content in the carbon materials. Using a UV laser with 355 nm wavelength, the oxygen content of the LIG material obtained was about 14%, while using a visible laser with 532 nm wavelength, the LIG material obtained had more oxygen functional groups and the oxygen content was about 25% (Fig. 4b).[61] The deoxygenation reaction of the infrared laser was less pronounced. UV and visible lasers also facilitate the conversion of biomass precursors without burning the material.[62] When the precursor is a cellulose-based material, the ablation rate of the material under a UV laser is very low.[46] Jung *et al.* demonstrated that a visible laser with 532 nm wavelength could effectively carbonize cellulose-based substrates (such as paper cups and paper bags) to produce LIG. This process was able to effectively prevent cellulosic paper ablation due to the fact that cellulosic paper exhibited a higher optical absorption in the visible range.[63] The selection of laser wavelength also determines the spatial resolution of the process. Compared with IR lasers, UV and visible lasers can achieve higher resolution due to their shorter wavelengths. Stanford *et al.* prepared micro-patterned LIG with a thickness below 5 μm and a resolution of approximately 12 μm using a 405 nm visible laser. In contrast, conventional CO_2 lasers (9.3 μm and 10.6 μm) exhibited spot sizes in the range of 60–120 μm, limiting the ability to prepare submicrometer fine patterns (Fig. 4c and d).[64] The dimensions of LIG generated using a 405 nm laser were reduced by at least 60%, and as small as one-tenth of the size of the materials prepared by IR lasers. These distinctions highlight the critical role of laser wavelength in optimizing LIBCs for specific applications.

Laser power. The intensity of laser power directly determines whether or not LIG can be successfully obtained. A laser with too low power does not provide enough energy to induce the complete carbonization of carbon precursors. If the laser power is too high, the structure of the formed LIG will be severely destroyed or even will be completely oxidized and ablated. Therefore, a reasonable range of laser power should be determined to acquire high-quality LIG, and the microstructure and composition of LIG are also influenced by the laser power.

Tour *et al.* used a CO_2 laser to turn pine wood into graphene (P-LIG) and investigated the effects of laser intensity between 10% and 90% on the morphology and structure of the formed materials (Fig. 5a and b).[31] No clear Raman signal was detected at 10% of laser power. Nevertheless, as the laser power increased to 30%, the pine began to transform into amorphous carbon with a broad D peak (1350 cm^{-1}) and a weak 2D peak (2700 cm^{-1}). As the laser power was increased from 50% to 90%, a contraction of the D and G peaks as well as an enhancement of the 2D peak were observed, indicating

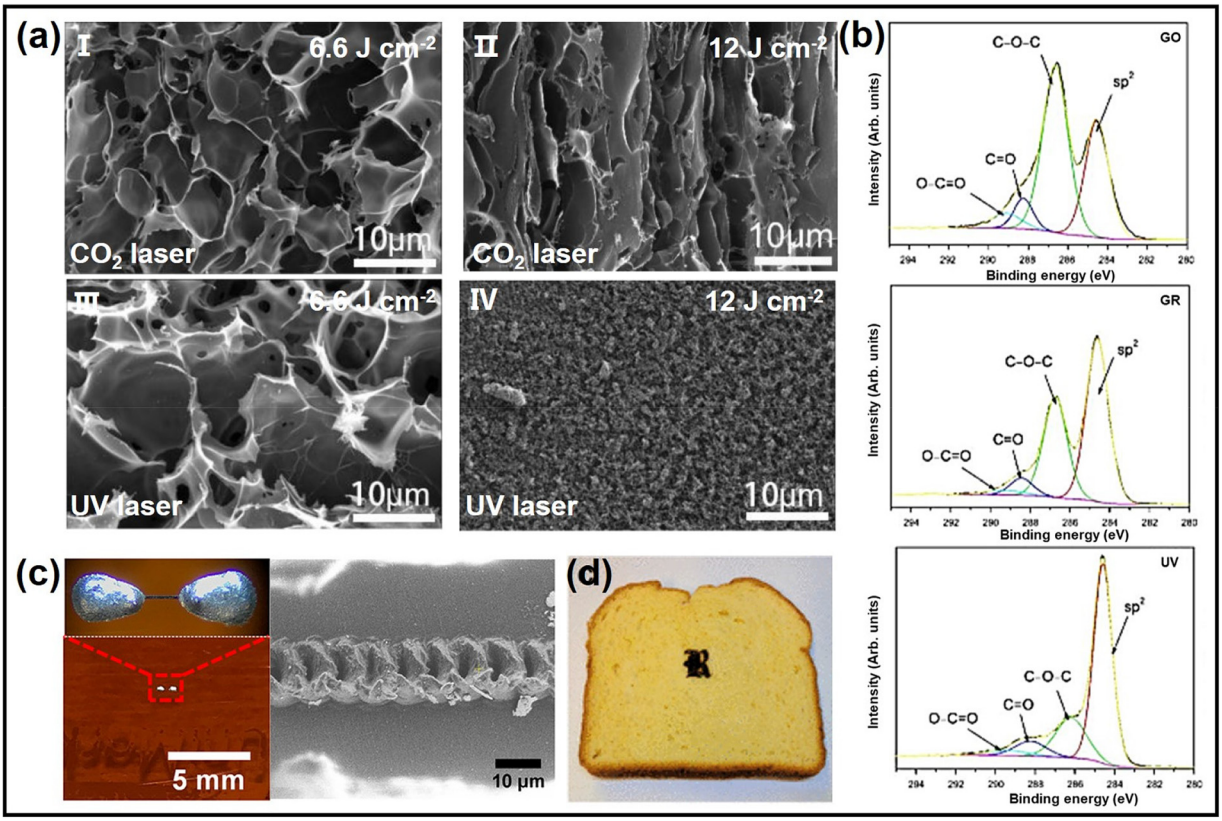

Fig. 4 (a) SEM images: (I) CO_2 laser of 6.6 J cm^{-2}, (II) CO_2 laser of 12 J cm^{-2}, (III) UV laser of 6.6 J cm^{-2}, (IV) UV laser of 12 J cm^{-2}.[60] (b) High-resolution XPS of C 1s for GO, GR-LIG, and UV-LIG.[61] (c) Optical image and SEM image of LIG patterns generated with 1 pixel width.[64] (d) Photo of LIG patterned on bread with a CO_2 laser.[46]

the formation of a graphene structure. Although the increased laser power yielded LIGs with higher quality, the wood overheated when the laser power reached 90%, resulting in inferior a LIG structure. Sun *et al.* prepared LIG materials from lignin-polyethersulfone (lignin-PES) film and found that their surface morphology changes with the laser power.[65] As shown in scanning electron microscopy (SEM) images (Fig. 5c), the surface of the original lignin-PES film was smooth. After the laser treatment, a shaggy morphology was observed, and as the laser power was increased from 6% to 15%, the thicknesses of the LIG-P*X* (*X* = 6%, 9%, 12%, 15%) materials were 204.5 μm, 321.4 μm, 388.9 μm, and 547.6 μm, making the volume of the LIG bigger. These results indicate that the graphene structure evolves gradually with the increase of laser power. For a given laser system and set of parameters, the laser power must exceed a certain threshold to form LIG. Lin *et al.* prepared various LIG materials at laser powers ranging from 2.4 W to 5.4 W with a fixed scanning speed of 3.5 mm s^{-1}.[27] It was found from Fig. 5d that the content of C atoms increased dramatically from an initial 71% to 97%, whereas the content of N and O atoms decreased dramatically to below 3% at 2.4 W of laser power, indicating that it is the threshold at which the graphene structure began to form. If the power continued to increase, the carbon content gradually decreased and the oxygen content somewhat increased, which is a result of the air-atmosphere treatment that tends to introduce oxygen-containing functional groups into graphene. As revealed in Fig. 5e, when below a power threshold of 2.4 W, PI was an insulator with a sheet resistance (R_s) above 90 MΩ m^{-2}, whereas from 2.4 W onwards, the R_s of the LIG decreased to below 35 Ω m^{-2}. As the laser power increased to 5.4 W, R_s gradually decreased to a minimum value (below 15 Ω m^{-2}), but the oxidation process began to adversely affect the film quality under this condition. These results further demonstrated that it was essential to select a suitable laser power to realize a high degree of graphitization of laser-induced carbon materials.[68]

Scanning speed. In order to improve the efficiency of laser-induced carbonization technology, it is also important to optimize the laser scanning speed. When the power density is certain, the magnitude of the laser scanning speed in turn determines the length of time that the precursor receives laser energy in the same location, which has a significant impact on the amount of heat absorbed by the target materials.

Lin *et al.* evaluated the effect of laser scanning speed on carbon conversion.[66] The laser scanning speed was selected below 3.5 mm s^{-1} and the laser power was set to 150 mW for preventing the damage of the nanolignin/cellulose nanofibril (LCNF) film. As the laser scanning speed decreased from 3.5 mm s^{-1} to 1 mm s^{-1}, stronger ablation of the film surface

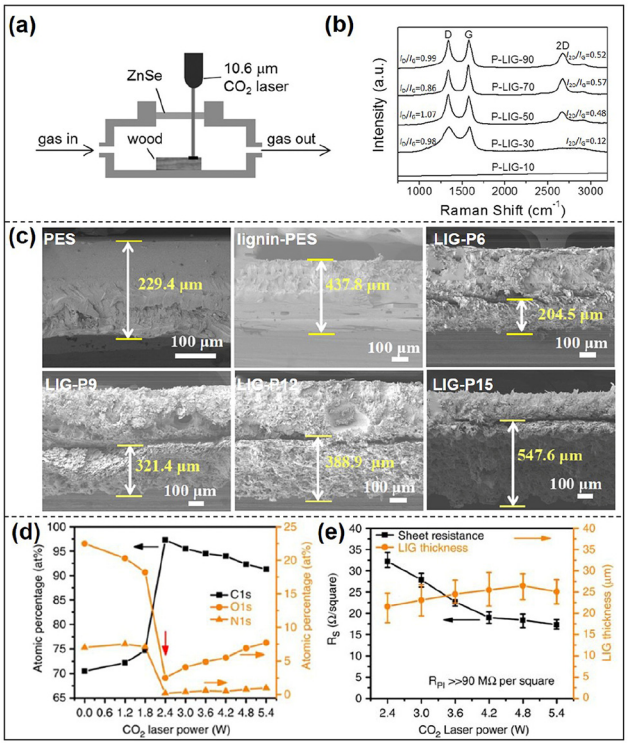

Fig. 5 P-LIG: (a) schematic illustration; (b) power-dependent Raman spectra.[31] Lignin-PES LIG: (c) cross-sectional SEM images of PES, lignin-PES, and lignin-PES LIG-P*X* (*X* = 6%, 9%, 12%, 15%).[65] LIG prepared at various laser powers: (d) atomic percentages of C, N, and O; (e) correlations of the R_s and LIG thicknesses.[27]

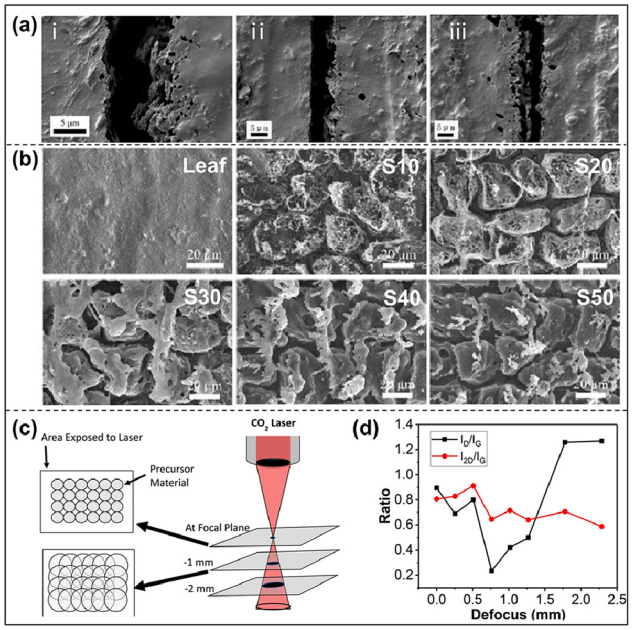

Fig. 6 LCNF: (a) SEM images at laser scanning speeds of (i) 1 mm s^{-1}, (ii) 2.5 mm s^{-1} and (iii) 3.5 mm s^{-1}.[66] FsLIG: (b) SEM images at different laser scanning speeds.[67] Lignin-derived LIG: (c) schematic of defocusing on the substrate to enlarge the laser spot size; (d) summary of I_D/I_G and I_{2D}/I_G ratios.[46]

occurred, and the width of the kerf was correspondingly increased from 5.6 μm to 9.2 μm due to the more heat accumulation on the surface (Fig. 6a). Kim *et al.* used a femtosecond laser to prepare graphene (FsLIG) from leaves.[67] It was concluded that the degree of heat accumulation is a key factor in converting leaves into graphene, and it is closely related to the laser scanning speed. That is, the properties of the obtained graphene can be controlled by modulating the scanning speed. Initially, a high scanning speed of 80 mm s^{-1} was used to act on the leaf. At this speed, no graphene was formed and the leaf was partially ablated. Then, the scanning speed was regulated between 10 mm s^{-1} and 50 mm s^{-1} to keep the heat accumulation at an optimal level. In combination with SEM images (Fig. 6b), when the scanning speed decreased from 50 mm s^{-1} to 10 mm s^{-1}, the pore structure of FsLIG became more and more abundant, which was mainly attributed to the rapid decomposition of the biomass components into gaseous products. The hierarchical porous structures can be obtained at low scanning speeds (10–20 mm s^{-1}).

Laser spot defocus. Multiple laser scribing or diffuse laser spot overlap scanning can accomplish what fixed-focus laser single scanning can't. The multiple laser scribing method can also be simplified to a defocused laser spot scanning method, allowing a single pass of the defocused laser spot scanning to produce high-quality LIG films. Chyan *et al.* pointed out that the laser beam has a conical shape, and different spot sizes can be achieved by varying the distance between the precursor material and the focal plane.[46] For the same position, the overlap of the defocused spots is equivalent to producing multiple exposures to the laser (Fig. 6c and d). As mentioned earlier, the direct laser-assisted treatment of biomass is more likely to result in the burning of biomass rather than the formation of LIG due to high laser energy in a single pass. However, biomass materials with a high lignin content (such as coconuts and potatoes) can be directly converted to LIG in air by the defocused laser spot scanning method.[69]

Atmosphere. One of the superiorities of laser-induced carbonization over other carbonization technologies is that carbon materials can be obtained under air. Meanwhile, the laser-processing atmosphere can be decisive to change the morphology and chemical composition of LIG and modulate the hydrophobicity and hydrophilicity of the surface, thus offering more possibilities for the functionalization of laser-induced carbon materials.[32] Tour's group processed PI membranes by laser scribing under different gas atmospheres (O_2, H_2, Ar, and air) (Fig. 7a).[70] As displayed in Fig. 7b, the contact angles of the LIG obtained under O_2 and air atmospheres were 0°, which correspond to the hydrophilic surface; and the contact angles of the LIG obtained under the atmospheres of reducing gases (H_2 or inert gases) were all larger than 150°, indicating their hydrophobicity. The hydrophilicity of LIG was related to its surface morphology and chemical composition. LIG prepared in an O_2 or air atmosphere exhibited a lamellar and striated mesoporous structure, whereas the hierarchical

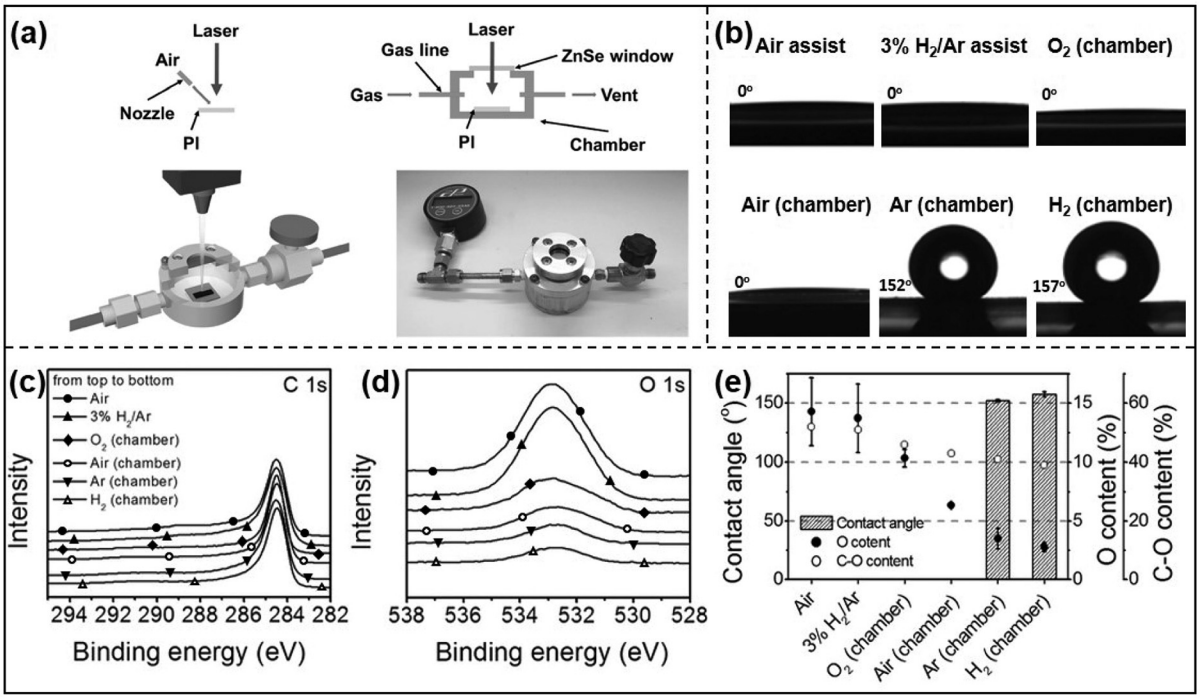

Fig. 7 LIG made under varying gas atmospheres: (a) schematics in a controlled atmosphere chamber; (b) water droplets on LIG surfaces; (c and d) high-resolution XPS of C 1s and O 1s; (e) relationship between water contact angle, O content, and C–O bond content.[70]

microporous structure and carbon nanoparticles can be observed from LIG prepared in Ar. The former favored in the promotion of hydrophilicity, and the latter was associated with the enhancement of the hydrophobicity of the surface. Furthermore, the LIG obtained in an O_2-containing atmosphere exhibited a higher O content and C–O bond content, endowing the LIG with strong hydrophilicity. In contrast, the LIG obtained in Ar or H_2 gas has a lower oxygen content and thus exhibits a stronger hydrophobicity and a higher contact angle (Fig. 7c–e). Thus, superhydrophilic or hydrophobic LIG can be obtained by changing the laser atmosphere and used for oil/water separation or micro-supercapacitors (MSCs).[71]

Modification of LIBCs

The physicochemical properties of carbon materials, including electrical conductivity, specific surface area, pore structure, surface chemistry, and composition, are closely related to their roles in specific applications. In general, LIBCs have excellent electrical conductivity and a developed porous structure, but are highly chemically inert, which extremely limits their application. In this regard, the doping of heteroatoms and the introduction of highly active components offer feasible solutions for activating LIBCs.

Chemistry modification

The doping of heteroatoms is considered as an efficient strategy to modulate the surface chemistry of carbon materials. Non-carbon atoms (such as N, O, S, P, and others) embedded in the carbon skeleton replace the position of some C atoms and thus change the electron cloud density, pore size, and surface acidity/base of carbon materials. Also, it can enrich the type and number of surface groups, generate more reactive sites, and improve the surface wettability.[72–74] Compared to in-furnace pyrolysis, laser-induced carbonization can produce carbon materials with a higher degree of graphitization, thereby improving the electrical conductivity of the materials. In addition, the types of N heteroatoms doped by laser-induced carbonization are mainly graphitic-N and pyridinic-N, which are favorable for the enhancement of electrical conductivity.[6,75,76] Another advantage of laser-induced carbonization is the ability to construct 3D interconnected foam structures without any special treatment. This structure significantly increases the specific surface area, enabling better interface contact with the electrolyte and thus improving the wettability.[77–79] All in all, carbon materials can exhibit more excellent electrical conductivity and electrolyte wettability, endowing them with more competitive edge in various applications. N,P co-doped LIG was prepared by a laser-induced strategy with cellulose nanofibers as carbon precursors and ammonium polyphosphate as the source of N and P (Fig. 8a).[80] XPS measurements were carried out to investigate the chemical composition of the surface of LIG. The four peaks at 398.7, 401.4, 402.0 and 403.7 eV in the N 1s XPS spectrum corresponded to pyrrolic nitrogen, pyridinic nitrogen, quaternary nitrogen, and oxidized nitrogen, respectively (Fig. 8b), and the two peaks at 131.4 eV and 132.2 eV in the P

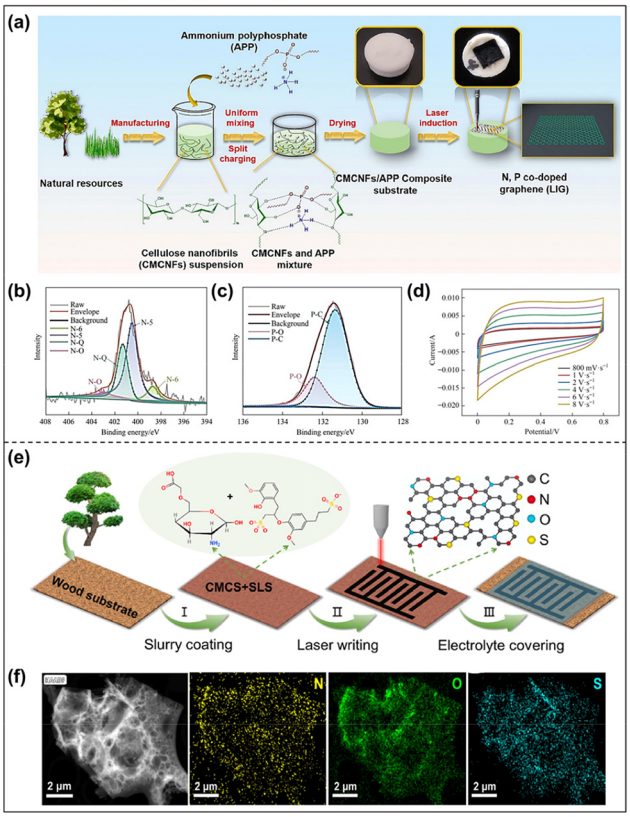

Fig. 8 N,P co-doped LIG: (a) synthesis schematics; (b and c) high-resolution XPS spectra of N 1s and P 1s; (d) CV curves at different scanning rates.[80] LIG-ONS: (e) schematic diagram; (f) HAADF-STEM images and elemental mapping images of N, O, and S.[81]

2p XPS spectrum corresponded to the P–C and P–O bonds, respectively (Fig. 8c). In addition, it was found that the micromorphology and pore structure of N,P co-doped LIG can be tuned by changing the number of laser passes. Benefiting from the abundant pores and the successful doping of N and P atoms, N,P co-doped LIG as the electrode of the supercapacitor displayed fast charge storage capability. As shown in Fig. 8d, with the increase of scanning rates, the integral area of the CV curves increased but their shapes did not change significantly. Yuan *et al.* prepared O/N/S co-doped graphene (LIG-ONS) by laser irradiation on the surface of carboxymethyl chitosan/sodium-lignosulfonate reinforced wood, in which wood was used as a renewable carbon source, carboxymethyl chitosan was adopted as a thickening agent and O/N dopant, and sodium-lignosulfonate was adopted as an O/S dopant (Fig. 8e).[81] The high angle angular dark field-scanning transmission electron microscopy (HAADF-STEM) image and the corresponding elemental mapping images showed a hierarchically porous structure and the uniform distribution of O, N, and S atoms in the graphene matrix (Fig. 8f), which were beneficial for the storage and transport of electrolyte ions. Therefore, the micro-supercapacitor based on the LIG-ONS electrode maintained a capacitance of 84.3% after 10 000 cycles with good cycling stability.

A duplicated laser scribing route was proposed to synthesize O/S co-doped porous graphene. As depicted in Fig. 9a, LIG was first obtained by the laser-induced carbonization of PI film. Then, sodium lignosulfonate slurry was prepared by dissolving it into hydroxyethyl cellulose (HEC) solution and was evenly coated on the LIG. After the second laser scribing, the sLIG-O/S14 electrode (the weight percentage of lignin in HEC solution was 14%) was obtained.[82] An undoped LIG electrode (labeled as LIG-S0) was also prepared by the laser treatment of HEC (without lignin)-coated LIG. As can be seen from Fig. 9b, LIG-S0 displayed a monotonous reticulated structure similar to pristine LIG, while sLIG-O/S14 presented foam-like structure surfaces embedded with interconnected macropores and an increased graphene thickness. It is worth noting that the content of S atoms was as high as 16.2 wt%, which was mainly in C–S–C and C–SO_x–C configurations (Fig. 9c). The nitrogen adsorption–desorption isotherms revealed that sLIG-O/S14 possessed abundant mesopores and macropores, and mesopores were dominant (Fig. 9d). Moreover, the specific surface area and pore volume of sLIG-O/S14 were higher than those of LIG-S0, which may be attributed to more structural defects induced by the doping of S atoms. O/S co-doping can not only facilitate the infiltration and transport of electrolytes, but also offer extra pseudocapacitance. As a consequence, sLIG-O/S14 achieved a better charge storage capability than LIG-S0. Another sulfur-doped porous graphene (L-P LIG) was prepared by laser direct writing on the lignin and polyethersulfone composite film. It was evidenced by XPS that S was doped into the graphene skeleton in the form of C–S–C and C═S bonding. Due to the hierarchical porous structure and the heteroatom (O and S) doping, the all-solid-state supercapacitor assembled with L-P LIG afforded a superhigh areal energy density of 1.53 mW h cm^{-2} at the areal power density of 25.4 mW cm^{-2}.[65]

Composition modification

Carbon materials are deemed as appealing hosts for metals or metal compounds due to their high specific surface area, developed porous structure, and high mechanical stability.[83] The composite methods of carbon and metal/metal compounds comprise *in situ* compositing and post-treatment. *In situ* compositing is realized by the co-pyrolysis of a carbon source and metal source, during which metal atoms tend to migrate and agglomerate into bulks due to their high surface energy. The post-treatment approaches suffer from a tedious and time-consuming process, and the interaction between the two components is inferior, which causes metal/metal compounds to be easily detached from the carbon substrate.[84] The above drawbacks are remedied simultaneously by laser-induced technology. The composites of carbon and metal/metal compounds can be obtained by direct laser treatment of carbon precursors containing metal sources.[85] Moreover, the instantaneous reaction conditions further inhibit the agglomeration of metal atoms. The laser-induced carbon and metal/metal compound composites have high electrical conductivity and ample adsorption/catalytic active sites, and thus show excellent application prospects in electronic or electrochemical devices.[20]

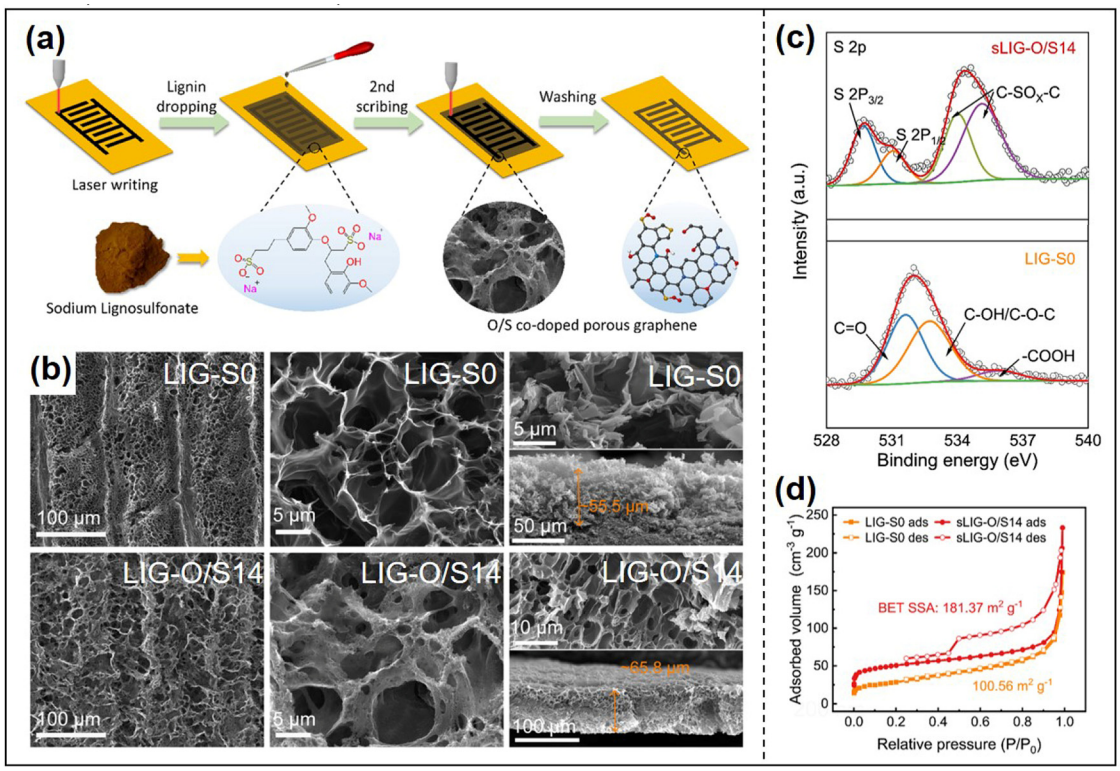

Fig. 9 sLIG-O/S electrode: (a) synthesis schematics; (b) SEM images; (c) high-resolution XPS spectra; (d) nitrogen adsorption–desorption isotherms.[82]

Tour *et al.* successfully prepared graphene embedded with various metal nanocrystals (cedar–LIG–M, M = Cu, Co, Ni, Fe, NiFe) by one-step laser scribing on the wood impregnated with metal salts under an Ar atmosphere (Fig. 10a).[86] The X-ray diffraction (XRD) and TEM results manifested that these metal alloy nanocrystals were homogeneously embedded into LIG (Fig. 10b and c). The I_D/I_G and I_G/I_{2D} ratios were in the range of 0.3–0.6 and 1.3–2.0, respectively, indicating a high degree of crystallinity of multilayered graphene (Fig. 10d). The as-made cedar–LIG–M composite exhibited outstanding electromagnetic interference shielding effectiveness and high electrocatalytic activity for oxygen evolution reaction (OER). Ying *et al.* prepared Au nanoparticle–3D graphene (AuNP–LIG) nanocomposites using laser-induced pyrolysis of PI substrates coated with a metal-chitosan gel (Fig. 10e).[87] Energy dispersive X-ray spectroscopy (EDX) elemental mapping indicated that the Au, C, N, and O elements were homogeneously distributed on the nanosheets, confirming the growth of AuNPs on the graphene surface (Fig. 10f). The immunosensor based on AuNP–LIG exhibited excellent properties such as low detection limit, high selectivity, and high flexibility (Fig. 10g).

Graphene decorated with Co_3O_4 nanoparticles (Co_3O_4 NPs/LIG) was synthesized by the laser treatment of cobalt nitrate-impregnated linden blocks in air (Fig. 11a).[88] The pristine linden wood showed a 3D porous structure, but the linden-derived LIG showed a loosely stacked laminar structure. The XRD revealed diffraction peaks corresponding to cubic Co_3O_4, demonstrating the incorporation of Co_3O_4 into LIG (Fig. 11b).

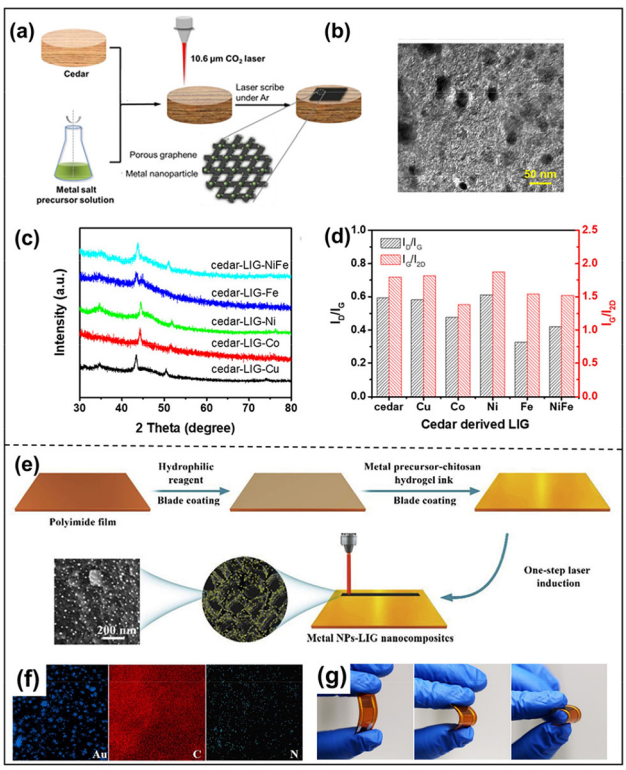

Fig. 10 Cedar–LIG–M: (a) synthesis schematics; (b) TEM image; (c) XRD patterns; (d) summary of I_D/I_G and I_G/I_{2D} ratios.[86] AuNP–LIG: (e) schematic diagram; (f) EDX elemental mapping images; (g) photographs of interdigitated electrodes under various bending states.[87]

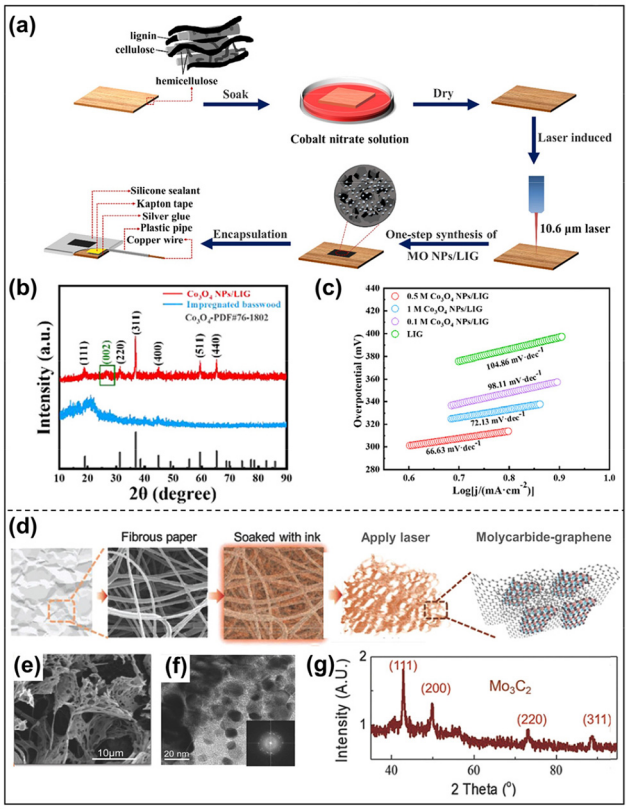

Fig. 11 Co_3O_4 NPs/LIG: (a) synthesis schematics; (b) XRD pattern; (c) Tafel diagram.[88] MCG: (d) schematic diagram; (e) SEM image; (f) TEM image; (g) XRD pattern.[89]

When used as the catalyst for OER, the required overpotential of the Co_3O_4 NPs/LIG composite was only 325 mV with a Tafel slope of 66.63 mV dec^{-1} at 10 mA cm^{-2}, while the LIG electrode required a high overpotential of 637 mV (Fig. 11c), which can be ascribed to that the uniformly dispersed Co_3O_4 nanoparticles provide more active sites. Zang *et al.* prepared molybdenum carbide–graphene (MCG) composites by direct-write laser patterning on fibrous paper soaked with gelatin ink containing Mo ions (Fig. 11d).[89] Elemental Mo played important roles in preventing the paper from burning and ensuring more carbon to be retained in the solid residue during MCG processing. It can be seen from the TEM images that MCG presented hierarchical pores with pore sizes ranging from hundreds of nanometers to several microns, and the size of molybdenum carbide nanoparticles is only around 10 nm (Fig. 11e and f). The XRD revealed the existence of Mo_3C_2 after the laser-induced conversion (Fig. 11g). The resulting MCG composites are mechanically stable and electrochemically active and can be utilized as conductive electrodes for various bendable electronics.

Applications of LIBCs

Micro-supercapacitors

The popularization and application of miniaturized and intelligent electronic products have stimulated the rapid development of MSCs with high power output and a long lifespan.[90,91] The fabrication of active materials and the design of electrode construction are of paramount importance. Carbon-based interdigitated electrodes facilitate electron transfer and shorten the ionic diffusion path, contributing to fast charge/discharge rates.[92] Among the current MSC fabrication methods, laser scribing technology can directly conduct the high-efficiency and high-resolution patterning on the surface of various film substrates, demonstrating strong device fabrication and system integration capabilities.[93]

A number of LIBCs have been reported as advanced MSC electrodes. Alshareef *et al.* fabricated lignin-derived LIG electrodes with hierarchical pores and an electrical conductivity of up to 66.2 S cm^{-1}.[94] When applied to MSCs, a high specific areal capacitance of 25.1 mF cm^{-2}, a volumetric energy density of 1 mW h cm^{-3}, and a volumetric power density of 2 W cm^{-3} were achieved. Kim *et al.* presented easy, maskless, and scalable laser writing on nature fallen leaves to directly fabricate highly conductive and hierarchical porous graphene materials (Fig. 12a).[67] The leave-derived LIG-MSC can easily power a light-emitting diode (LED) (Fig. 12b) and exhibited an outstanding areal capacitance (34.68 mF cm^{-2} at 5 mV s^{-1}). Martins *et al.* proposed the preparation of LIG from paper (Fig. 12c).[95] Before laser irradiation, the paper was impregnated with a flame retardant to prevent ablation under the laser beam. The paper-derived LIG exhibited a low sheet resistance of 30 Ω sq^{-1}. The paper-derived LIG-MSC yielded a specific capacitance of 4.6 mF cm^{-2} at 0.015 mA cm^{-2}. In addition, the device exhibited excellent cycling stability and good mechanical properties after 10 000 cycles at 0.5 mA cm^{-2}

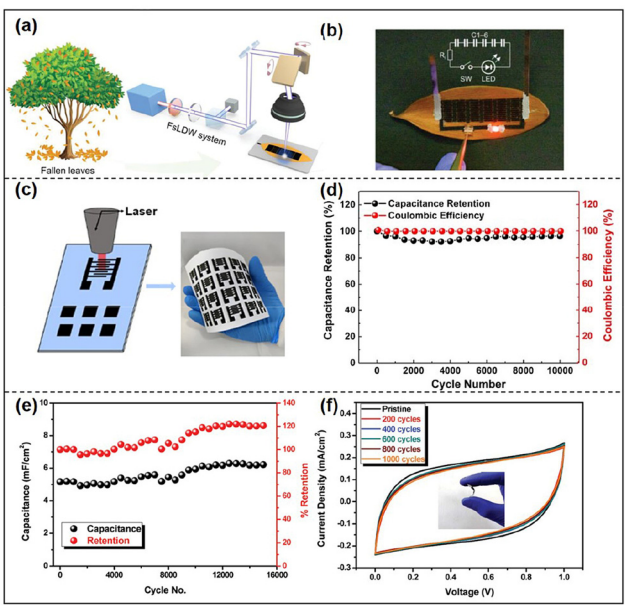

Fig. 12 Leave-derived LIG electrode: (a) synthesis schematics; (b) LED light-up.[67] Paper-derived LIG electrode: (c) synthesis schematics; (d) cycling stability at 0.5 mA cm^{-2}.[95] Mushroom-derived LIG electrode: (e) cycling stability at 0.05 mA cm^{-2}; (f) CV curves at 20 mV s^{-1} with various bending cycles.[96]

(Fig. 12d). Moreover, Ogale *et al.* converted biomass mushrooms into mesoporous carbon materials with a specific surface area of 2604 m^2 g^{-1}.[96] The mushroom-derived LIG-MSC had a high cycling stability of up to 15 000 cycles (Fig. 12e) and a high energy density (1.8 mW cm^{-2}). In addition, the CV curves after 1000 bends at an angle of 60° almost overlapped with the initial CV curves (Fig. 12f).

The doping of heteroatoms into the carbon matrix is beneficial for improving the electrical conductivity and electrolyte wettability and provides pseudo-capacitance contribution.[97] Yuan *et al.* applied the prepared O/N/S co-doped porous graphene for wood-derived LIG-MSC with an excellent areal capacitance of 82.1 mF cm^{-2} at 0.1 mA cm^{-2} and a corresponding high energy density of 7.3 μW h cm^{-2}.[81] In addition, the wood-derived LIG-MSC had good cycling stability (84.3% capacitance maintained after 10 000 cycles) and good modular integration capability (Fig. 13a–c). This group also patterned S-doped graphene on the surface of the sodium lignosulfonate-coated polyethersulfone film.[98] The corresponding lignin-derived LIG-MSC provided an ultra-high surface capacitance of 55.4 mF cm^{-2} and excellent cycling stability with 85.2% capacitance retention after 12 000 cycles, as well as excellent mechanical flexibility (Fig. 13d and e).

Similar work was also carried out by Iacopino' group.[99] The oak wood substrate was treated with H_3BO_3 and then carbonized to B-doped LIG. A sandwich-type B-doped LIG-MSC was assembled (Fig. 14a), and its areal capacitance could reach 11.24 mF cm^{-2} at 0.1 mA cm^{-2} (Fig. 14b). The device also showed excellent stability over time, with no significant loss of capacitance after 10 000 cycles (Fig. 14c). Besides, the introduction of highly active materials, typically metal compounds, can significantly enhance the charge storage capability of MSCs.[100] As shown in Fig. 14d, lignin, PAN, and MoS_2 were first mixed well to form a solution, and then the lignin/PAN/MoS_2 fiber (LF/MoS_2) membranes were manufactured by electrospinning with heat treatment at 450 °C.[101] Finally, the LF/MoS_2 membrane was scribed with a laser to obtain a LIG and MoS_2 composite (LLF/MoS_2-450). Owing to the presence of MoS_2, the capacitance of a MSC based on LLF/MoS_2-450 was increased from 391.2 F g^{-1} to 527.8 F g^{-1} at 1 A g^{-1} (Fig. 14e). Moreover, the device achieved a power density of 500 W kg^{-1} and an energy density of 73 W h kg^{-1}. Bending and cycling tests also showed good flexibility and a long service life for the e-textile (Fig. 14f).

Batteries

Lithium-ion batteries (LIBs) have dominated the secondary battery market for decades due to their high energy density,

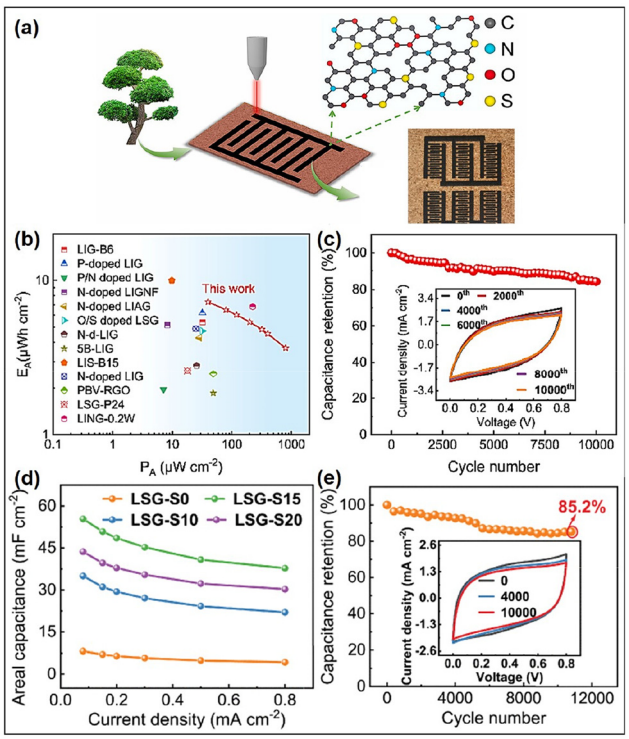

Fig. 13 Wood-derived LIG electrode: (a) synthesis schematics; (b) Ragone plots; (c) cycling stability at 50 mV s^{-1}, inset: comparison of CV curves after various cycles.[81] Lignin-derived LIG: (d) correlation of areal capacitance with varying current densities; (e) cycling stability at 50 mV s^{-1}, inset: comparison of CV curves after various cycles.[98]

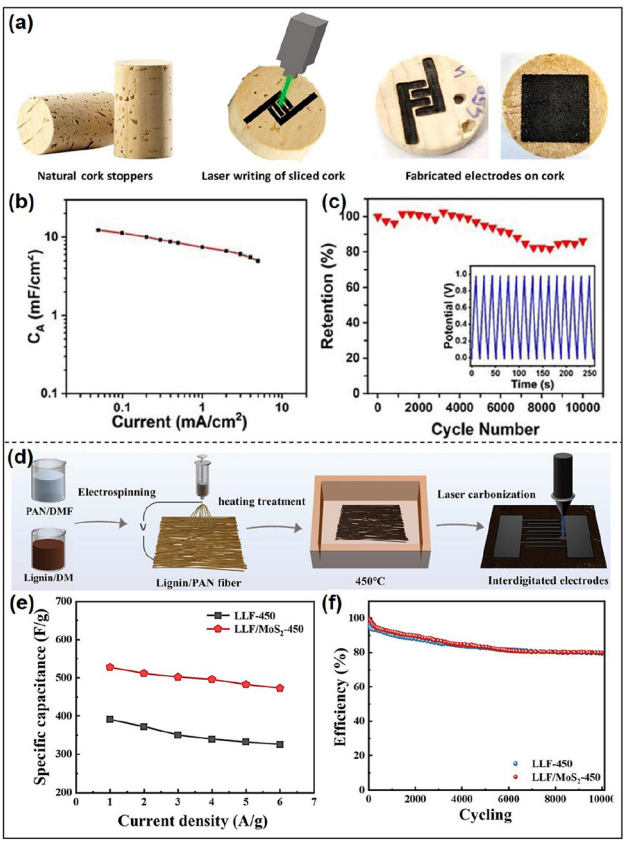

Fig. 14 Oak-derived LIG electrode: (a) synthesis schematics; (b) capacitance at different current densities; (c) cycling stability at 1 mA cm^{-2}.[99] LLF/MoS_2-450 electrode: (d) synthesis schematics; (e) specific capacitance at different current densities; (f) cycling stability at 20 A g^{-1}.[101]

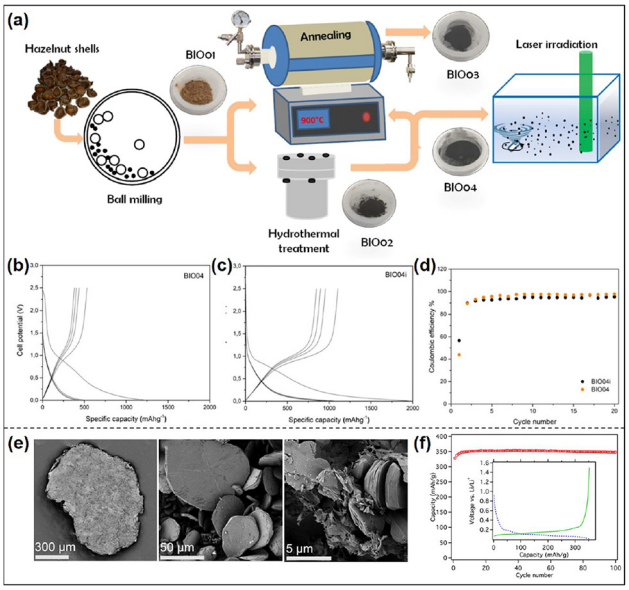

Fig. 15 Hazelnut-derived BIO04 and BIO04i electrodes: (a) synthesis schematic; (b and c) galvanostatic charge/discharge curves; (d) coulombic efficiency during cycling at 10 mA g^{-1}.[108] Lignocellulose-derived graphene electrode: (e) SEM images; (f) cycling stability at 500 mA g^{-1}.[109]

long lifespan, and no memory effect.[102–104] However, the sluggish diffusion kinetics of lithium ions in conventional bulk graphite anodes results in a limited rate capacity of LIBs, which hinders their application in high-magnification devices. Currently, three-dimensional LIG materials with a high specific surface area and porous structure have been demonstrated to provide a rapid electron transfer network and shorten the lithium-ion diffusion distance, thus significantly improving the rate and cycling performances of LIBs.[105–107]

Teghil's group discovered that the laser-induced carbonization technique could further enhance the properties of biomass-derived carbon anode materials.[108] They first performed hydrothermal treatment on biomass hazelnuts, followed by laser-induced carbonization in acetonitrile to obtain carbon materials with different morphologies and properties (Fig. 15a). The specific surface area of the hydrothermally treated carbon material (BIO04) was only 382 m^2 g^{-1}, and the laser-induced carbon material (BIO04i) presented a high specific surface area of 760 m^2 g^{-1}. When utilized as the anode material of LIBs, BIO04 showed a severe capacity loss in the early cycles, with an initial coulombic efficiency of only 44% at 700 mA h g^{-1} and a capacity retention of 42% after the 20th cycle, whereas BIO04i showed an initial coulombic efficiency of 56% and a capacity retention of 52% after the 20th cycle (Fig. 15b–d). The enhancement of electrochemical perform-

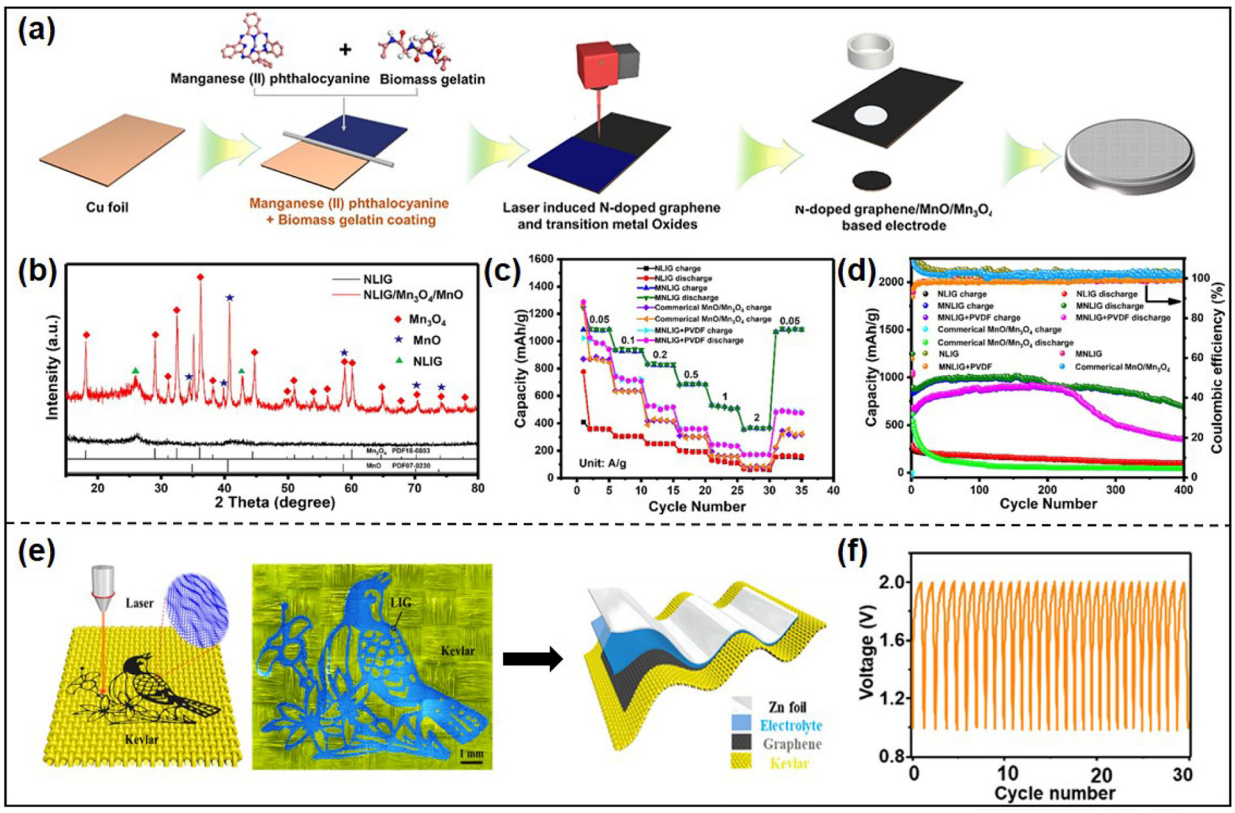

Fig. 16 MNLIG anode material for LIBs: (a) synthesis schematic; (b) XRD pattern; (c) rate performances at 0.05–2 A g^{-1}; (d) cycling performances.[110] The graphene/Kevlar textile cathode for Zn–O_2 batteries: (e) synthesis schematic; (f) galvanostatic discharge–charge curves during cycling at 1 mA cm^{-2}.[111]

ances may be attributed to the increase of specific surface area. Wagner *et al.* converted lignocellulose into flake graphene by a two-step process of pyrolytic carbonization followed by laser carbonization (Fig. 15e).[109] When flake graphene was applied as the anode material for LIBs, it showed an initial coulombic efficiency of up to 84% and lost only 1% of its capacity over 100 cycles at 500 mA g^{-1} (Fig. 15f).

The *in situ* combination of laser-induced graphene and metal oxides can impede the agglomeration and stacking of graphene sheets, thus increasing the specific surface area and facilitating electronic and ionic transport. As the carrier of a highly active metal oxide, graphene can induce the uniform nucleation, growth, and formation of metal oxides, favoring the full exposure of active sites.[112] Zhang *et al.* prepared MnO/Mn_3O_4/N doped graphene (MNLIG) by the laser irradiation of a gelatin substrate containing manganese phthalocyanine (Fig. 16a).[110] The successful incorporation of MnO/Mn_3O_4 particles was demonstrated by XRD (Fig. 16b). The MNLIG anode material achieved an initial coulombic efficiency of 67.3%, an excellent rate capacity of 365 mA h g^{-1} at 2 A g^{-1} and a high reversible capacity of 992 mA h g^{-1} at 0.2 A g^{-1} (Fig. 16c). After 400 cycles, it retained 83.6% of capacity, demonstrating excellent cycling stability (Fig. 16d).

Zinc–air batteries (ZABs) have gathered burgeoning interest because of their good safety and low price, but the charging and discharging efficiencies and long cycling stability of zinc–air batteries are still inferior, which is mainly related to the slow electrochemical oxygen reduction reaction. Therefore, highly active catalysts are urgently needed. Zhang *et al.* patterned the graphene structure on the surface of Kevlar textiles.[111] The resulting graphene/Kevlar textile showed high mechanical strength and huge application potential for flexible ZABs (Fig. 16e). Co_3O_4 was then introduced into graphene/Kevlar textiles to further improve the electrochemical performances of ZABs. The as-made Co_3O_4-graphene/Kevlar textile cathode exhibited better catalytic activity for OER with a high open-circuit voltage (1.37 V), as well as excellent cycling stability during 30 cycles at 1 mA cm^{-2} (Fig. 16f).

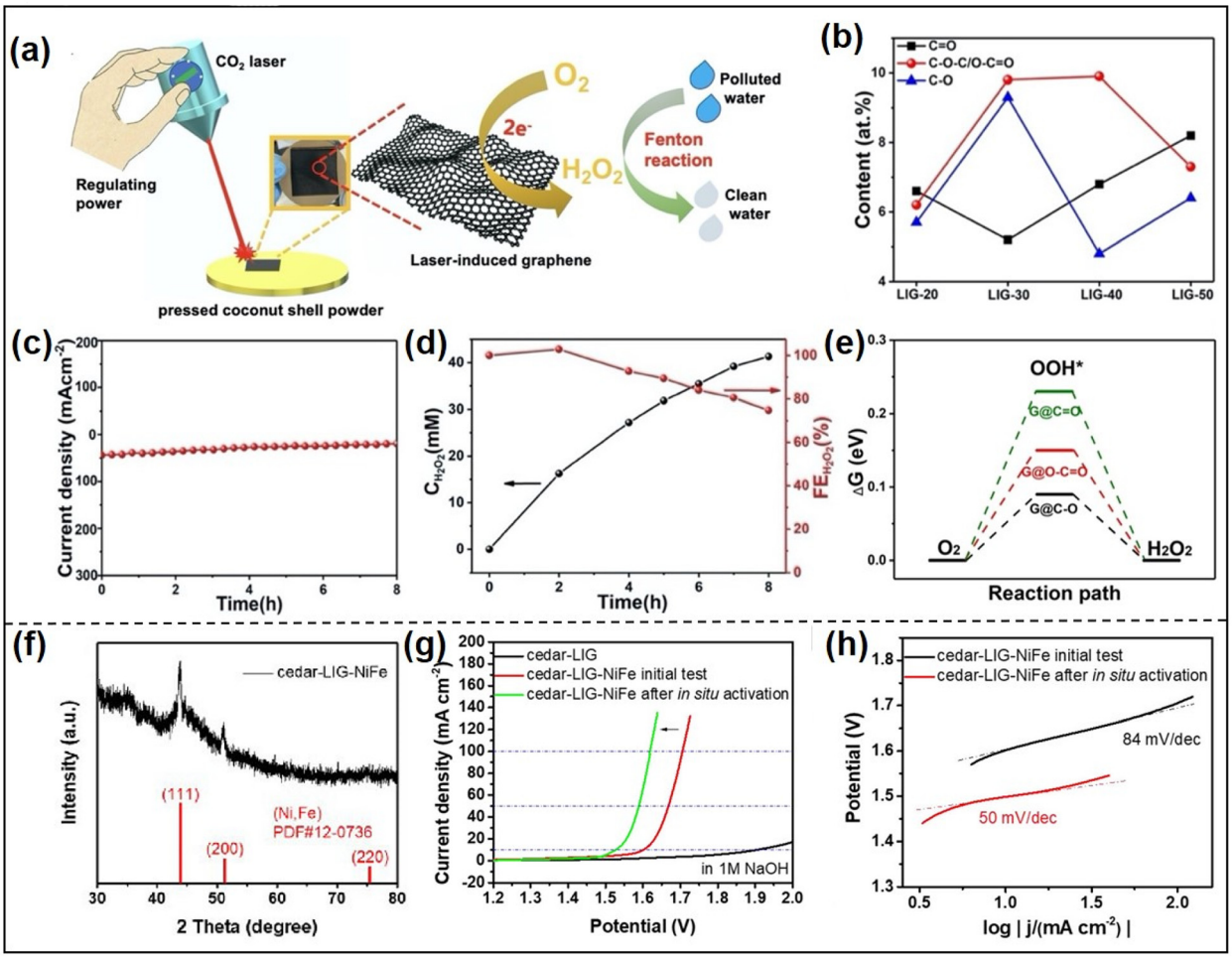

Fig. 17 Coconut shell-derived LIG catalyst for ORR: (a) synthesis schematic; (b) variation of oxygen species with laser power; (c) amperometric response at 50 mA cm^{-2}; (d) $FE_{H_2O_2}$ and H_2O_2 concentration during 8 h test; (e) free energy diagram on three models.[115] The cedar–LIG–NiFe catalyst for OER: (f) XRD pattern; (g) polarization curves; (h) Tafel slopes.[86]

Electrocatalysts

LIBC-based catalysts have demonstrated promising applications in electrocatalytic reactions, such as the hydrogen evolution reaction (HER), the oxygen reduction reaction (ORR), and the OER. The conversion efficiency of these electrocatalytic reactions is highly dependent on the activity level of the catalyst and the number of active sites.[113] The modification of heteroatoms or functional groups can break the equilibrium of the original electronic structure of the carbon matrix and enhance the interaction with reactants, so the purpose of improving the catalytic activity of LIBC-based catalysts is achieved.[114] For example, coconut shell-derived LIG was prepared (Fig. 17a) and its oxygen species were modulated by adjusting the laser power (Fig. 17b).[115] The as-obtained LIG with ample C–O and O–C=O species showed outstanding catalytic activity in the two-electron ORR. During the 8 h test period, the current density remained almost unchanged (Fig. 17c). Besides, the H_2O_2 concentration increased linearly with the reaction time and the Faraday efficiency (FE) was more than 78%, which indicated a stable catalytic activity. Additionally, the concentration of H_2O_2 was up to 41 mM in 100 mL electrolyte after 8 h of testing, higher than most of the carbon-based electrocatalysts (Fig. 17d). Finally, in combination with the DFT calculations, it was also demonstrated that C–O and O–C=O species are the key active sites for high catalytic performance (Fig. 17e).

Carbon materials can also serve as the firm support to tightly anchor highly active metal catalysts, which is beneficial for the full exposure of active sites and the high stability of the catalysts.[116] As mentioned previously,[86] an ultrasound-assisted and laser-induced carbonization method was proposed to successfully fabricate a cedar–LIG–NiFe composite, as evidenced by the XRD results (Fig. 17f). The electrocatalytic properties of cedar–LIG–NiFe were then investigated in 1 M NaOH aqueous solution. The results of linear scanning voltammetry showed that the introduction of the NiFe alloy greatly improved the catalytic activity of cedar–LIG–NiFe, and the electrode had a low overpotential of 296 mV for OER at 10 mA cm^{-2} (Fig. 17g). It was seen from the Tafel plots that cedar–LIG–NiFe had a smaller Tafel slope and higher current density, indicative of a better OER performance (Fig. 17h). Wang *et al.* synthesized Ru and N co-doped porous graphene (Ru@CN) by the laser treatment of honey containing $RuCl_3$ for pH-generic HER.[117] The electrocatalytic activity of Ru@CN was optimized by tuning the loading of Ru and the laser power. Benefiting from the abundant Ru^0 and Ru–N sites, the Ru@CN catalyst with 2.66 wt% of Ru loading exhibited superior catalytic activity and excellent HER durability under different pH conditions. Especially in alkaline solution, it exhibited a smaller overpotential of 11 mV at 10 mA cm^{-2}.

Sensors

A sensor is an element that converts a range of external signals into electrical signals. It requires sensing materials with high electrical, thermal, and electronic transfer ability to respond sensitively to stimuli from external fields.[118–120] LIBCs have been considered to be one of the most promising materials for electrical sensing due to their high electronic mobility, easy functionalization, and good flexibility.

A variety of small molecules such as lactic acid, dopamine (DA), and H_2O_2 can be detected in electrochemical biosensors based on LIBCs. Meng *et al.* demonstrated a green route for the conversion of lignin into graphene by sequential laser lithography,[121] followed by water stripping and sodium borohydride ($NaBH_4$) treatment (Fig. 18a). The electrochemical lactate biosensor was then fabricated based on lignin-derived LIG and exhibited excellent response to lactate in artificial sweat (pH = 6.5). It showed a well-defined current response to a dynamic concentration range of lactate up to 18 mM, and reached a stable current value within 20 s (Fig. 18b). In addition, the electrode also exhibited an excellent shelf life. If the biosensor was stored in a refrigerator (4 °C) for 8 weeks, the response deviated from the initial response value by 5% during the first two weeks (Fig. 18c). Mahmood *et al.* demonstrated the conversion of biomass-based films consisting of kraft lignin and cellulose nanofibers (CNF/KL) into porous graphene (Fig. 18d).[122] The 3D structure of CNF/KL-derived LIG enhanced the electrochemical response because of its high specific surface area and conductive pathways capable of

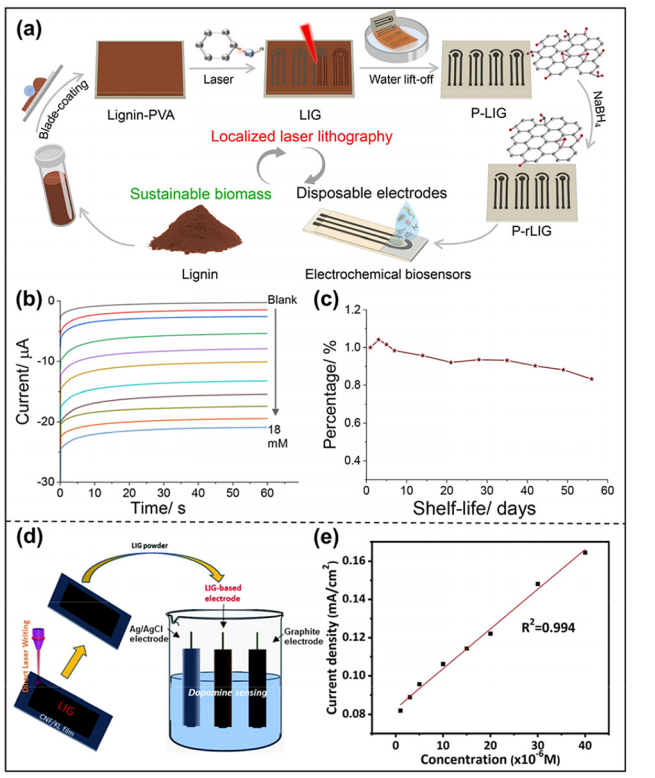

Fig. 18 Electrochemical lactate biosensor based on lignin-derived LIG: (a) synthesis schematics; (b) amperometric response; (c) shelf-life evaluation of 6 mM lactate.[121] An electrochemical DA biosensor based on CNF/KL-derived LIG: (d) synthesis schematics; (e) correlation of the oxidation peak current density and concentration.[122]

efficient charge transfer and mass transfer. The electrochemical sensor was fabricated based on the CNF/KL-derived LIG electrode for the DA detection by varying the scanning speed and keeping the DA concentration constant at 1 mM. The corresponding calibration curve showed that the increase in current density was quasi-reversible, and the device linearly detected DA at concentrations ranging from 5 to 40 μM with a sensitivity of 4.39 μA μM^{-1} cm^{-2} (Fig. 18e), indicating its great potential for ultrasensitive detection of DA and other biomolecules. Zhang *et al.* also synthesized porous graphene by implementing a direct laser-writing technique on lignocellulosic biomass, which was fabricated into a DA sensor.[123] The prominent oxidation peak appeared when tested with 1 mM DA. The sensor exhibited an extremely high sensitivity (2080 μA mM^{-1} cm^{-2}) with the limit of detection of 0.659 × 10^{-6} M.

LIBCs have also been used in humidity sensors, strain sensors, and temperature sensors. For example, Yang *et al.* used the laser-induced carbonization technique to convert waste grapefruit peels into LIG (Fig. 19a).[124] After that, the humidity sensor was fabricated by utilizing GO as a humidity-sensitive material coated on the peel-LIG. The relative humidity (RH) tests at different frequencies indicated that the capacitance of the humidity sensor increased more significantly at lower frequencies (Fig. 19b). Therefore, testing was conducted at a lower frequency of 1000 Hz. The sensing performance was evaluated by measuring its capacitance in a controlled environment with varying RH. The results showed that the capacitance increased drastically from 1.315 pF to 2200 pF as the RH increased from 40% to 90%, yielding a high sensitivity of 4397.37 pF per RH (Fig. 19c). This can be attributed to the fact that GO is hyper-permeable to water molecules, and the absorbed water molecules enhanced the polarization of GO, which in turn increased its dielectric constant. Kim *et al.* fabricated green and flexible temperature sensors based on naturally dried thin leaves, without significant damage after laser carbonization, and the resulting graphene had a porous structure (Fig. 19d).[125] The temperature sensor based on leave-derived LIG exhibited fast response and recovery performance. When tested at temperatures between 25 and 50 °C, the response time and the recovery time were 7.0 and 6.2 s, respectively. Such a high heat transfer efficiency can be attributed to the low electrical resistance of LIG (Fig. 19e). Kulyk *et al.* carbonized filter paper to LIG with a thin-layer resistance as low as 32 Ω sq^{-1}.[126] The paper-derived LIG was applied to mechanical strain sensors and retained high stability for more than 21 h (Fig. 19f). In addition, the sensor was also fixed to the underside of the flexible plastic support and subjected to a three-point bending test, showing that the resistance of the sensor increased as the bending radius decreased (Fig. 19g).

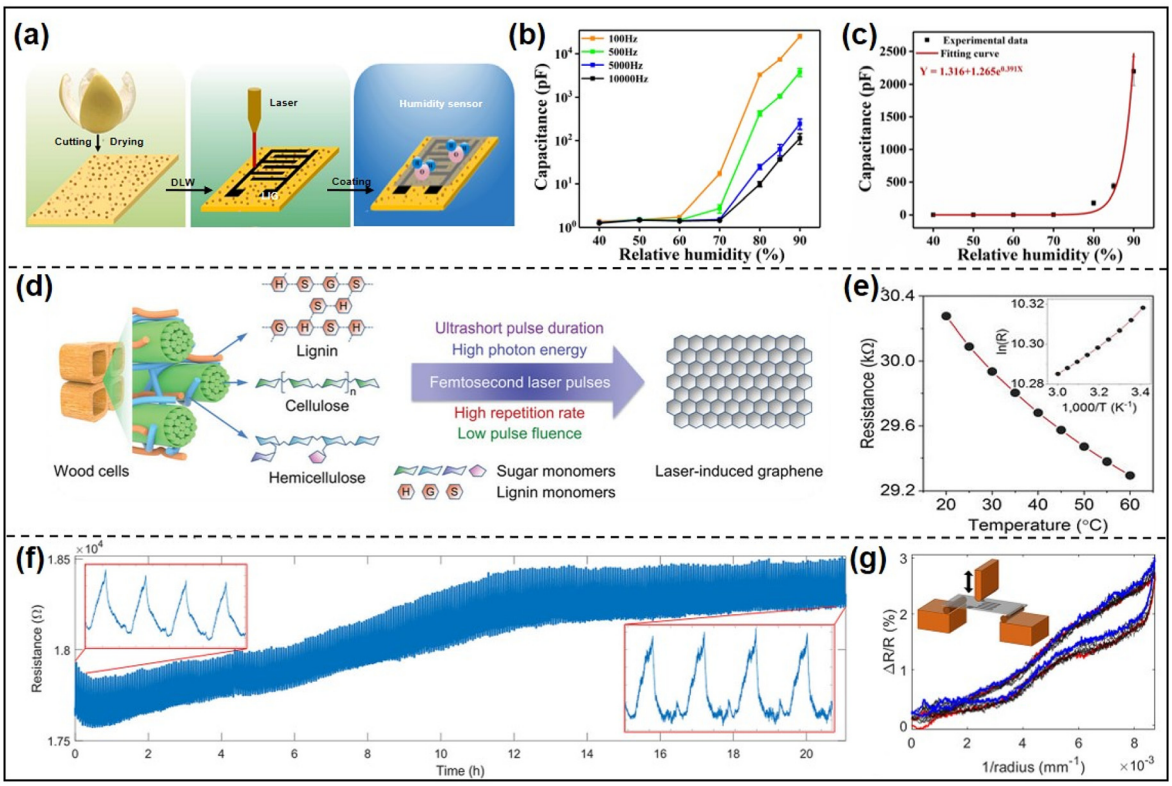

Fig. 19 Humidity sensor based on peel-LIG: (a) synthesis schematics; (b) capacitance responses to varying RH at various frequencies; (c) capacitance responses to varying RH.[124] A temperature sensor based on leave-derived LIG: (d) synthesis schematics; (e) resistance measured at different temperatures.[125] A strain sensor based on paper-derived LIG: (f) long-time measurement; (g) resistance variation as a function of inverse bend radius.[126]

Other applications

Beyond energy storage and sensing, LIBC materials have demonstrated substantial potential across diverse advanced applications. In dye adsorption, Liu *et al.* developed a hierarchically porous carbon material (PCP) by CO_2 laser carbonization of sodium lignosulfonate-modified cellulose paper, achieving a customizable structure with a high surface area and tunable surface chemistry (Fig. 20a and b).[127] This PCP exhibited exceptional adsorption capacity for methylene blue dye (~0.21 g g^{-1}), retaining high efficiency and reusability across multiple recycling cycles (Fig. 20c). This surpassed traditional powdered or granular carbon adsorbents, facilitating simpler pollutant removal system assembly and efficient adsorbent recycling. In water purification, Ye *et al.* engineered a LIG layer on wood to form a multilayer system, integrating a superhydrophilic bottom layer, natural wood microchannels, and a hydrophobic top layer (Fig. 20d).[128] This configuration effectively prevented salt accumulation and bacterial contamination while enabling the removal of hydrophobic organics in solar-driven water treatment. The porous LIG layer accelerated water evaporation, achieving 110% solar-to-heat conversion efficiency, over 99.9% removal of metal ions, and greater than 90% organic removal under high-salinity conditions (Fig. 20e). This demonstrated a promising approach for energy-efficient, environmentally sustainable water purification and wastewater treatment. LIBC materials are also advancing in energy harvesting. Soin *et al.* constructed a friction nanogenerator (TENG) using paper-based LIG electrodes, achieving a peak output voltage of 625 V, a charge density of 138 μC m^{-2}, and a power density of 2.25 W m^{-2}, which surpassed traditional aluminum electrodes by approximately 150% (Fig. 20f–h).[129] The improved performance was attributed to the low interfacial impedance and well-matched Fermi level of LIG. These

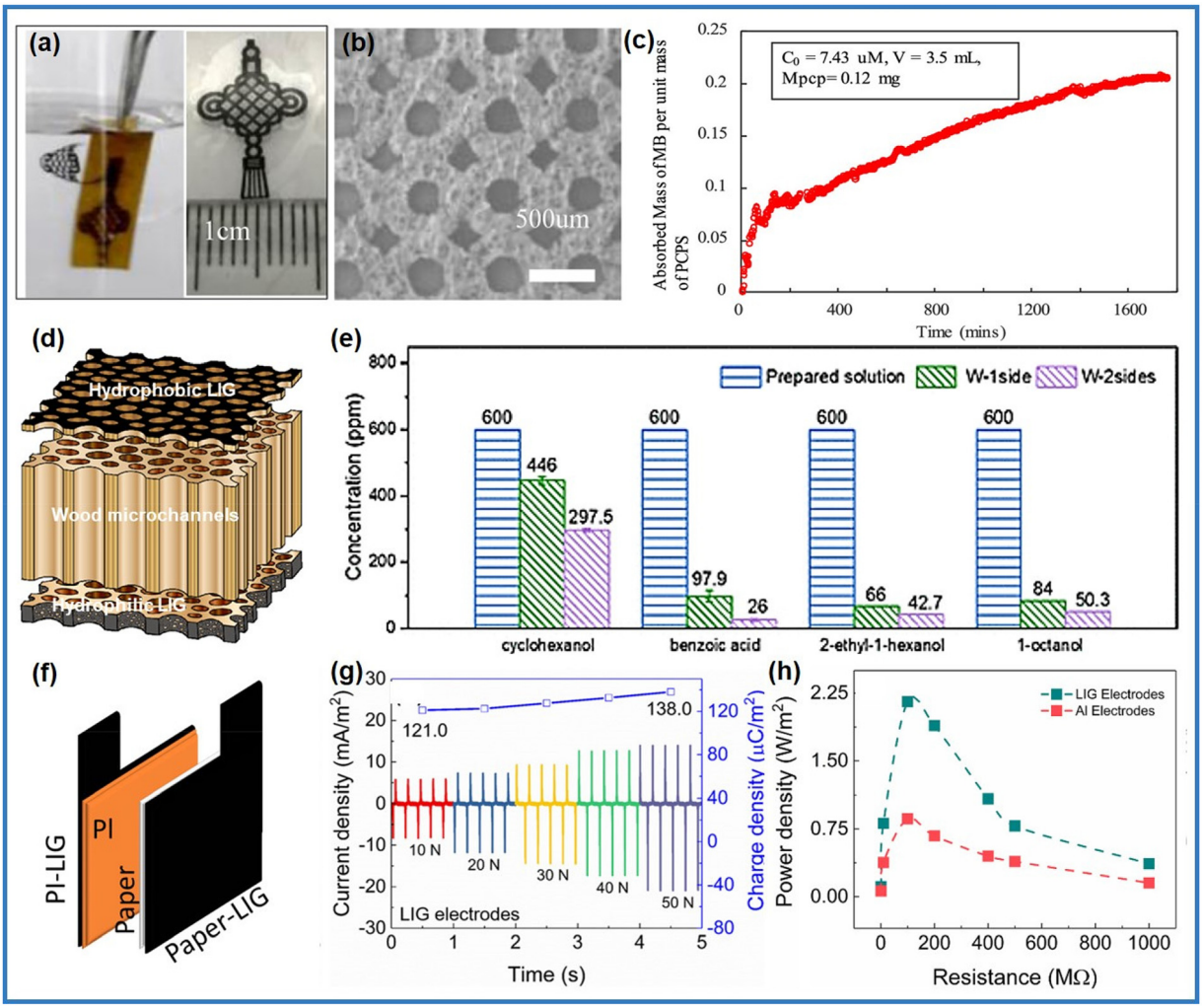

Fig. 20 PCP: (a) photo of a Chinese-knot-shaped PCP; (b) SEM image; (c) mass adsorption kinetics of methylene blue dye by unit mass.[127] Wood-derived LIG: (d) hierarchically structured interfacial evaporation system; (e) concentration column of organic matter.[128] Paper-derived LIG: (f) schematics of the PI-Paper TENG; (g) the corresponding charge density under various current responses; (h) power density measured with variable load resistance.[129]

Table 2 The precursor types, laser processing conditions, and applications of LIBCs

Starting materials		Laser parameters				Resulting carbon-based materials		Application	
Biomass	Additive agent	Wavelength	Laser power	Scanning speed	Atmosphere	Product	Device	Performance	Ref.
Lignin	Au	10.6 μm	1.8 W	57.1 mm s^{-1}	Air	Au-LIG	MSC	25.1 mF cm^{-2} at 0.1 mA cm^{-2}	94
Wood	Chitosan/sodium lignosulphonate	10.6 μm	8.2 W	80 mm s^{-1}	Air	O/N/S-co-doped LIG	MSC	82.1 mF cm^{-2} at 0.1 mA cm^{-2}	81
Sodium lignosulfonate	Polyethersulfone	10.6 μm	8.2 W	80 mm s^{-1}	Air	S-doped porous LIG	MSC	55.4 mF cm^{-2} at 0.08 mA cm^{-2}	98
Cork	H_3BO_3	450 nm	0.9 W	3 mm s^{-1}	Air	B-doped LIG	MSC	11.24 mF cm^{-2} at 0.1 mA cm^{-2}	99
Mushroom	—	10.6 μm	4.8 W	—	Air	3D porous LIG	MSC	11.3 mF cm^{-2} at 0.2 mA cm^{-2}	96
Paper	Borax	10.6 μm	3 W	7.6 cm s^{-1}	Air	LIG	MSC	4.6 mF cm^{-2} at 0.015 mA cm^{-2}	95
Cedar wood	Ni/Fe metal nanocrystals	10.6 μm	8 W	15 cm s^{-1}	Ar	LIG-NiFe	OER	Overpotential of 296 mV at 10 mA cm^{-2}	86
Coconut shells	—	10.6 μm	25 W	3 mm s^{-1}	Ar	Oxygen-enriched LIG	ORR	High Faraday efficiency (>78%)	115
Honey	$RuCl_3$	10.6 μm	6 W	100 mm s^{-1}	Air	Ru and N co-doped LIG	HER	Overpotential of 11 mV at 10 mA cm^{-2}	117
Jellyfish	Silicon nanoparticles	450 nm	2.8 W	20 mm s^{-1}	Air	Si-doped LIG	LIBs	High coulombic efficiency (>99%)	130
Wood powder	—	1300 nm	10 W	—	Air	Flake-potato graphite	LIBs	353 mA h g^{-1} at 0.5 A g^{-1}	84
Hazelnut shell	Acetonitrile	532 nm	5.6 W	—	Air	N-doped LIG	LIBs	Coulombic efficiency (>59%)	108
Gelatin	Mn^{2+} phthalocyanine	10.6 μm	3.8 W	35 cm s^{-1}	Air	MnO/Mn_3O_4/N-LIG	LIBs	992 mA h g^{-1} at 0.2 A g^{-1}	110
Textile	—	10.6 μm	6.5 W	50 mm s^{-1}	Air	Kevlar-textile LIG	ZAB	High open-circuit voltage of 1.37 V	111
Leaves	—	517 nm	7.8 W	2 mm s^{-1}	Air	2D patterning LIG	ES, SC	Long response time of 27.2 s	125
Kraft lignin	Cellulose nanofibers	10.6 μm	28 W	20 cm s^{-1}	Air	Defect-rich LIG	ES	High sensitivity of 4.39 μA $μM^{-1}$ cm^{-2}	122
Pomelo peels	—	10.6 μm	9 W	40 mm s^{-1}	Air	Porous LIG	ES, PS, OS	Limit of detection (10–5 M)	124
Paper	—	10.6 μm	1.5 W	38.1 cm s^{-1}	Ar	Porous LIG	ES, PS	High sensitivity of 4.39 mA mM^{-1} cm^{-2}	131
Cellulose	—	10.6 μm	5 W	40 mm s^{-1}	Air	Porous LIG	PS	High sensitivity of 27.24 μA mm^{-1}	132
Paper	—	10.6 μm	3.6 W	3 mm s^{-1}	Air	3D porous LIG	TENG	High power output of 2.25 W m^{-2}	129
Cellulose paper	Sodium lignosulfonate	10.6 μm	20 W	100 mm s^{-1}	Air	Porous LIG	Adsorbents	Adsorption capacity of 0.21 g g^{-1}	127
Wood	—	10.6 μm	5 W	10 mm s^{-1}	Air	Porous LIG	Water purification	Energy conversion efficiency of 110%	128

characteristics made LIG-based TENGs promising candidates for high-efficiency energy harvesting and self-powered devices. In sum, LIBC materials present extensive application potential, from sustainable pollutant removal to advanced electronics and energy solutions, paving the way for innovation in addressing current environmental and energy challenges.

Conclusions and outlooks

This review summarizes the research progress of LIBCs from fundamentals to applications. Laser-induced carbonization technology has been shown to be a facile and high-efficiency strategy to pattern high-precision carbon structures on the surface of various biopolymer substrates. The microstructures and properties of LIBCs can be regulated by tuning biomass-containing precursor types and laser processing conditions to satisfy the demands for application in micro-supercapacitors, batteries, electrocatalysis, sensors, and so on (Table 2). Although some progress has been made, the research on LIBCs is still in infancy, and there are many intractable challenges that need to be addressed in the future. Because of the complex molecular structure of biomass, the extreme carbonization condition induced by laser irradiation, and the intricate mutual impacts of diverse laser parameters, the comprehensive formation mechanism of LIBCs is still under debate, and the common laws on the correlation between biomass precursor, laser parameters, and carbon structure are still lacking. Hence, advanced *in situ* techniques, such as *in situ* infrared spectroscopy, *in situ* X-ray absorption spectroscopy, *in situ* mass spectrometry and *in situ* SEM, are expected to comprehensively reveal the effects of laser penetration depth on biomass substrates, as well as their molecular and microstructural evolution during the laser-induced carbonization. In addition, machine learning is a high-efficiency method to predetermine the suitability of laser processing conditions, which will be helpful for offering a universal guidance strategy for the controllable preparation of LIBCs.

At present, the types of biomass precursors for laser processing are limited, and the functionalization of LIBCs is not sufficiently developed. The attention to LIBCs is mainly focused on the pore structure, specific surface area, and electrical conductivity. In the future, it is necessary to further expand the types of precursors and refine the composition and structure of precursors with a view to fabricating a wider variety of LIBCs. Moreover, much effort should be devoted to developing laser-induced technology for the controllable construction of a defect structure, metal single-atom coordination structure, and heterostructure in LIBC-based materials. There is also a need to broaden the application scope of LIBCs, such as lithium–sulfur batteries, lithium–air batteries, sodium-ion batteries, multifunctional sensors, water treatment, and so on.

Biomass usually contains unwanted elements, impurities, and contaminants that may find their way into the final biomass-derived carbon product. The quality of LIBCs can be improved by the pretreatment of biomass, but this will inevitably increase the cost and procedures and may cause environmental problems. The poor homogeneity of the biomass precursor and the high sensitivity of laser processing to operating environments lead to changes in the properties of LIBCs in different batches. Besides, it is also worth trying to introduce flame-retardant functional groups into biomass, which can effectively prevent ablation during the laser carbonization process, thereby improving the quality of LIBCs. In addition, the production of LIBCs is still at the laboratory stage. In the future, low-cost, high-quality, and large-scale production techniques are in high demand, and an all-in-one integrated system should be developed to enable the commercial implementation of LIBCs. More detailed comparative LCA studies on the environmental impact and economic benefits of laser-induced carbonization are necessary in the future, which will help to quantify the actual benefits of laser-induced carbonization.

More challenges bring about more opportunities. The unparalleled advantages of laser-induced technology towards biomass-derived carbon-based materials, coupled with the vigorous development of advanced energy storage devices and intelligent devices, are significantly encouraging researchers from diverse fields to engage in this research. It is anticipated that substantial breakthroughs will be made in this field in the near future. We hope that this review can provide comprehensive understanding and fresh inspiration on the controllable preparation and cutting-edge applications of LIBCs.

Author contributions

Xingjie Xu: writing – original draft, conceptualization, writing – review & editing, and validation. Mengdi Zhang: writing – original draft, conceptualization, writing – review & editing, funding acquisition, and supervision. Chao Qi: supervision. Yi Sun: writing – original draft, validation, and writing – review & editing. Lijun Yang: writing – original draft. Xin Gu: writing – original draft. Yanpeng Li: conceptualization and supervision. Mingbo Wu: funding acquisition and supervision. Bin Wang: conceptualization, writing – review & editing, and supervision. Han Hu: conceptualization, funding acquisition, and supervision.

Data availability

The datasets used during the current study are available from the corresponding author upon reasonable request.

Conflicts of interest

There are no conflicts to declare.

Acknowledgements

This work was supported by the National Natural Science Foundation of China (22138013, 22005341, 22309206), the

National Key Research and Development Program (2023YFB4203702, 2023YFB4203703), the Shandong Provincial Excellent Young Scientists Fund Program (Overseas) (2024HWYQ-047), the Taishan Scholars Program of Shandong Province (tsqn20221121, tsqn20221117) and the Independent Innovation Research Project of China University of Petroleum (22CX06026A).

References

1 Y. Dong, Q. Wang, H. Wu, Y. Chen, C.-H. Lu, Y. Chi and H.-H. Yang, *Small*, 2016, **12**, 5376–5393.
2 C. Y. Chaparro-Garnica, E. Bailón-García, A. Davó-Quiñonero, D. Lozano-Castelló and A. Bueno-López, *Chem. Eng. J.*, 2022, **432**, 134218.
3 B. Zheng, X. Lin, X. Zhang, D. Wu and K. Matyjaszewski, *Adv. Funct. Mater.*, 2020, **30**, 1907006.
4 L. Li, L. Wang, T. Ye, H. Peng and Y. Zhang, *Small*, 2021, **17**, 2005015.
5 G. Liao, F. He, Q. Li, L. Zhong, R. Zhao, H. Che, H. Gao and B. Fang, *Prog. Mater. Sci.*, 2020, **112**, 100666.
6 M. Devi, H. Wang, S. Moon, S. Sharma and V. Strauss, *Adv. Mater.*, 2023, **35**, 2211054.
7 H. Zhang, Y. Zhang, L. Bai, Y. Zhang and L. Sun, *J. Mater. Chem. A*, 2021, **9**, 12521–12552.
8 W. Zhao, Q. Ge, H. Li, N. Jiang, S. Yang and H. Cong, *Green Chem.*, 2024, **26**, 8550–8563.
9 S. Zago, L. C. Scarpetta-Pizo, J. H. Zagal and S. Specchia, *Electrochem. Energy Rev.*, 2024, **7**, 1.
10 Y. Feng, J. Jiang, Y. Xu, S. Wang, W. An, Q. Chai, U. H. Prova, C. Wang and G. Huang, *Carbon*, 2023, **211**, 118105.
11 H. Zhang, K. Yang, Y. Tao, Q. Yang, L. Xu, C. Liu, L. Ma and R. Xiao, *Biotechnol. Adv.*, 2023, **69**, 108262.
12 H. He, R. Zhang, P. Zhang, P. Wang, N. Chen, B. Qian, L. Zhang, J. Yu and B. Dai, *Adv. Sci.*, 2023, **10**, 2205557.
13 R. P. Singh, R. Yadav, V. Pandey, A. Singh, M. Singh, K. Shanker and P. Khare, *Biochar*, 2024, **6**, 17.
14 Z. Wang, D. Shen, C. Wu and S. Gu, *Green Chem.*, 2018, **20**, 5031–5057.
15 H. Deng, Z. Wang, M. Kim, Y. Yamauchi, S. J. Eichhorn, M.-M. Titirici and L. Deng, *Nano Energy*, 2023, **117**, 108914.
16 G. Singh, R. Bahadur, A. M. Ruban, J. M. Davidraj, D. Su and A. Vinu, *Green Chem.*, 2021, **23**, 5571–5583.
17 B. Zhang, Y. Jiang and R. Balasubramanian, *J. Mater. Chem. A*, 2021, **9**, 24759–24802.
18 M. Graglia, J. Pampel, T. Hantke, T.-P. Fellinger and D. Esposito, *ACS Nano*, 2016, **10**, 4364–4371.
19 A. M. Schwenke, S. Hoeppener and U. S. Schubert, *Adv. Mater.*, 2015, **27**, 4113–4141.
20 S. Bai, L. Ruan, H. Chen, Y. Du, H. Deng, N. Dai and Y. Tang, *Chem. Eng. J.*, 2024, **493**, 152805.
21 F. L. P. Veenstra, N. Ackerl, A. J. Martín and J. Pérez-Ramírez, *Chem*, 2020, **6**, 1707–1722.
22 H. Guo, J. Xie, G. He, D. Zhu, M. Qiao, J. Yan, J. Yu, J. Li, Y. Zhao, M. Luo and H. Han, *Nano Res.*, 2024, **17**, 6212–6230.
23 L. Cheng, C. S. Yeung, L. Huang, G. Ye, J. Yan, W. Li, C. Yiu, F.-R. Chen, H. Shen, B. Z. Tang, Y. Ren, X. Yu and R. Ye, *Nat. Commun.*, 2024, **15**, 2925.
24 S. D. Janssens, D. Vázquez-Cortés, B. Sutisna and E. Fried, *Carbon*, 2023, **215**, 118455.
25 S. Gao, Y. Zhu, Y. Gong, Z. Wang, W. Fang and J. Jin, *ACS Nano*, 2019, **13**, 5278–5290.
26 Z. Yang, X. Yang, T. Yang, Y. Cao, C. Zhang, Y. Zhang, P. Li, J. Yang, Y. Ma and Q. Li, *Energy Storage Mater.*, 2023, **54**, 51–59.
27 J. Lin, Z. Peng, Y. Liu, F. Ruiz-Zepeda, R. Ye, E. L. G. Samuel, M. J. Yacaman, B. I. Yakobson and J. M. Tour, *Nat. Commun.*, 2014, **5**, 5714.
28 S. P. Singh, Y. Li, J. Zhang, J. M. Tour and C. J. Arnusch, *ACS Nano*, 2018, **12**, 289–297.
29 X. Zang, N. Ferralis and J. C. Grossman, *ACS Nano*, 2022, **16**, 2101–2109.
30 H. Zhang, Q. Li, K. D. Hammond, X. He, J. Lin and C. Wan, *Green Chem.*, 2024, **26**, 5921–5932.
31 R. Ye, Y. Chyan, J. Zhang, Y. Li, X. Han, C. Kittrell and J. M. Tour, *Adv. Mater.*, 2017, **29**, 1702211.
32 K. Avinash and F. Patolsky, *Mater. Today*, 2023, **70**, 104–136.
33 S. P. Lee, P. S. Chee, C. H. Tan, K. F. Chong, E. H. Lim and C. Guan, *Chem. Eng. J.*, 2024, **499**, 156110.
34 T. Pinheiro, M. Morais, S. Silvestre, E. Carlos, J. Coelho, H. V. Almeida, P. Barquinha, E. Fortunato and R. Martins, *Adv. Mater.*, 2024, **36**, 2402014.
35 C.-C. Kung, B. A. McCarl and X. Cao, *Energy Policy*, 2013, **60**, 317–323.
36 Y. Wang, M. Zhang, X. Shen, H. Wang, H. Wang, K. Xia, Z. Yin and Y. Zhang, *Small*, 2021, **17**, 2008079.
37 B. Yang, J. Dai, Y. Zhao, J. Wu, C. Ji and Y. Zhang, *Biochar*, 2022, **4**, 51.
38 T.-S. D. Le, H.-P. Phan, S. Kwon, S. Park, Y. Jung, J. Min, B. J. Chun, H. Yoon, S. H. Ko, S.-W. Kim and Y.-J. Kim, *Adv. Funct. Mater.*, 2022, **32**, 2205158.
39 C. Martinez-Smit, M. Bastidas-Barranco, F. Chejne and M. García-Pérez, *Energy Fuels*, 2022, **36**, 12475–12490.
40 J. Tar and J. Grenthe, *Independent thesis Advanced level (degree of Master (Two Years))*, Thesis, Linköping University, 2024.
41 Z. Zhang, H. Zhu, W. Zhang, Z. Zhang, J. Lu, K. Xu, Y. Liu and V. Saetang, *Carbon*, 2023, **214**, 118356.
42 L. Zhang, Z. Zhou, X. Hu and L. Wen, *J. Semicond.*, 2023, **44**, 031701.
43 C. T. Long, J. H. Oh, A. D. Martinez, C. I. Sanchez, A. Sarmah, K. Arole, M. T. Rubio and M. J. Green, *Carbon*, 2022, **200**, 264–270.
44 Y. Dong, S. C. Rismiller and J. Lin, *Carbon*, 2016, **104**, 47–55.
45 A. Vashisth, M. Kowalik, J. C. Gerringer, C. Ashraf, A. C. T. van Duin and M. J. Green, *ACS Appl. Nano Mater.*, 2020, **3**, 1881–1890.

46 Y. Chyan, R. Ye, Y. Li, S. P. Singh, C. J. Arnusch and J. M. Tour, *ACS Nano*, 2018, **12**, 2176–2183.
47 M. Zhang, C. Yu, Z. Ling, J. Yu, S. Li, C. Zhao, H. Huang and J. Qiu, *Green Chem.*, 2019, **21**, 2095–2103.
48 R. Ye, D. K. James and J. M. Tour, *Adv. Mater.*, 2019, **31**, 1803621.
49 Q.-M. Huang, H. Yang, S. Wang, X. Liu, C. Tan, A. Luo, S. Xu, G. Zhang and H. Ye, *ACS Appl. Nano Mater.*, 2023, **6**, 10453–10465.
50 H. Wang, S. Delacroix, O. Osswald, M. Anderson, T. Heil, E. Lepre, N. Lopez-Salas, R. B. Kaner, B. Smarsly and V. Strauss, *Carbon*, 2021, **176**, 500–510.
51 H. Wang, M. Jerigova, J. Hou, N. V. Tarakina, S. Delacroix, N. López-Salas and V. Strauss, *J. Mater. Chem. A*, 2022, **10**, 24156–24166.
52 R. Senga, Y.-C. Lin, S. Sinha, T. Kaneko, N. Okoshi, T. Sasaki, S. Morishita, H. Sawada, S. T. Park and K. Suenaga, *Microsc. Microanal.*, 2021, **27**, 2344–2345.
53 H. Wahab, V. Jain, A. S. Tyrrell, M. A. Seas, L. Kotthoff and P. A. Johnson, *Carbon*, 2020, **167**, 609–619.
54 Y. Peng, J. Cao, Y. Sha, W. Yang, L. Li and Z. Liu, *Light: Sci. Appl.*, 2021, **10**, 168.
55 Y. Li, T. Wu, Y. Wang, J. Li, W. Yu, G. Zhang, B. Chang, L. Zhao, H. Liu and W. Zhou, *SusMat*, 2023, **3**, 533–542.
56 J. Mu, M. Zhang, Y. Li, Z. Dong, Y. Pan, B. Chen, Z. He, H. Fang, S. Kong, X. Gu, H. Hu and M. Wu, *Nano Res.*, 2023, **16**, 12304–12314.
57 R. Wu, M. T. Gilavan, M. A. Akbar, L. Fan and P. R. Selvaganapathy, *Carbon*, 2024, **216**, 118597.
58 M. Khandelwal, C. V. Tran, J. Lee and J. B. In, *Chem. Eng. J.*, 2022, **428**, 131119.
59 J. Cai, C. Lv and A. Watanabe, *Nano Energy*, 2016, **30**, 790–800.
60 L. Wang, Z. Wang, A. N. Bakhtiyari and H. Zheng, *Micromachines*, 2020, **11**, 1094.
61 J. Gaidukevič, R. Trusovas, A. Sartanavičius, R. Pauliukaitė, G. Niaura, M. Kozłowski and J. Barkauskas, *Mater. Res. Bull.*, 2024, **178**, 112916.
62 A. C. Bressi, A. Dallinger, Y. Steksova and F. Greco, *ACS Appl. Mater. Interfaces*, 2023, **15**, 35788–35814.
63 Y. Jung, J. Min, J. Choi, J. Bang, S. Jeong, K. R. Pyun, J. Ahn, Y. Cho, S. Hong, S. Hong, J. Lee and S. H. Ko, *Appl. Mater. Today*, 2022, **29**, 101589.
64 M. G. Stanford, C. Zhang, J. D. Fowlkes, A. Hoffman, I. N. Ivanov, P. D. Rack and J. M. Tour, *ACS Appl. Mater. Interfaces*, 2020, **12**, 10902–10907.
65 X. Sun, X. Liu and F. Li, *Appl. Surf. Sci.*, 2021, **551**, 149438.
66 Y. Lin, Q. Zhang, Y. Deng, K. Shen, K. Xu, Y. Yu, S. Wang and G. Fang, *ACS Sustainable Chem. Eng.*, 2021, **9**, 3112–3123.
67 T.-S. D. Le, Y. A. Lee, H. K. Nam, K. Y. Jang, D. Yang, B. Kim, K. Yim, S.-W. Kim, H. Yoon and Y.-J. Kim, *Adv. Funct. Mater.*, 2022, **32**, 2107768.
68 M. Y. Kumar and A. Borenstein, *Carbon*, 2022, **199**, 208–214.
69 J. T. Li, K. M. Wyss, W. Chen, J. Chen, B. Deng, J. L. Beckham, P. A. Advincula, P. E. Savas, V. D. Li, O. Jin and J. M. Tour, *Carbon*, 2023, **215**, 118494.
70 Y. Li, D. X. Luong, J. Zhang, Y. R. Tarkunde, C. Kittrell, F. Sargunaraj, Y. Ji, C. J. Arnusch and J. M. Tour, *Adv. Mater.*, 2017, **29**, 1700496.
71 D. C. Marcano, D. V. Kosynkin, J. M. Berlin, A. Sinitskii, Z. Sun, A. Slesarev, L. B. Alemany, W. Lu and J. M. Tour, *ACS Nano*, 2010, **4**, 4806–4814.
72 M. Fan, J. Cui, J. Wu, R. Vajtai, D. Sun and P. M. Ajayan, *Small*, 2020, **16**, 1906782.
73 B. Yang, Y. Guan, Y. Lu and Z. Chu, *Mater. Lett.*, 2024, **366**, 136505.
74 C. Chen, Z. Jiang, Y. Bai, M. Zhai, F. Jia, W. Hai, M. Li, J. Jiang, H. Shao, G. Shao, N. Chen and S. Bi, *Chem. Eng. J.*, 2024, **489**, 151275.
75 F. Wang, X. Dong, K. Wang, W. Duan, M. Gao, Z. Zhai, C. Zhu and W. Wang, *Carbon*, 2019, **150**, 396–407.
76 H. Wang, T. Maiyalagan and X. Wang, *ACS Catal.*, 2012, **2**, 781–794.
77 H. Liu, Y. Zheng, K.-S. Moon, Y. Chen, D. Shi, X. Chen and C.-P. Wong, *Nano Energy*, 2022, **94**, 106902.
78 R. Li, J. Song, S. Zhi, X. Wang, L. Wang, K. Jiang and D. Wu, *Desalination*, 2023, **548**, 116286.
79 Q. Fan, C. Song and P. Fu, *J. Cleaner Prod.*, 2024, **452**, 142169.
80 J. Wei, W. Yang, S. Jia, J. Wei and Z. Shao, *Chin. J. Chem. Eng.*, 2022, **47**, 31–38.
81 M. Yuan, Z. Wang, Y. Rao, Y. Wang, B. Gao, J. Yu, H. Li and X. Chen, *Carbon*, 2023, **202**, 296–304.
82 M. Yuan, F. Luo, Y. Rao, Y. Wang, J. Yu, H. Li and X. Chen, *J. Power Sources*, 2021, **513**, 230558.
83 R. Ye, Z. Peng, T. Wang, Y. Xu, J. Zhang, Y. Li, L. G. Nilewski, J. Lin and J. M. Tour, *ACS Nano*, 2015, **9**, 9244–9251.
84 H. Liu, Z. Sun, Y. Chen, W. Zhang, X. Chen and C. P. Wong, *ACS Nano*, 2022, **16**, 10088–10129.
85 Y. Wang, Y. Zhao, X. Li, L. Jiang and L. Qu, *Adv. Funct. Mater.*, 2022, **32**, 2203164.
86 X. Han, R. Ye, Y. Chyan, T. Wang, C. Zhang, L. Shi, T. Zhang, Y. Zhao and J. M. Tour, *ACS Appl. Nano Mater.*, 2018, **1**, 5053–5061.
87 Z. You, Q. Qiu, H. Chen, Y. Feng, X. Wang, Y. Wang and Y. Ying, *Biosens. Bioelectron.*, 2020, **150**, 111896.
88 J. Li, X. Yu, R. Sun, H. Li, X. Zhu, Y. Ma and L. Ma, *Carbon Trends*, 2023, **12**, 100285.
89 X. Zang, C. Shen, Y. Chu, B. Li, M. Wei, J. Zhong, M. Sanghadasa and L. Lin, *Adv. Mater.*, 2018, **30**, 1800062.
90 S. Seo, I. H. Oh and S. T. Chang, *Small*, 2024, **20**, 2311726.
91 S. Li, M. Zhang, Z. Feng, Y. Huang, T. Qian, H. Hu, X. Zheng, P. Liu, H. Liu, T. Xing and M. Wu, *Chem. Eng. J.*, 2021, **424**, 130315.
92 Y. Zhang, H. Zhang, X. Wang, X. Shi, Z. Zhao, Y. Wang, J. Liu, C. Tang, G. Wang and L. Li, *Energy Environ. Mater.*, 2024, **7**, e12681.

93 X.-D. Zhu, C.-Y. Ren, Y. Liang, X. Liang, N. Lu, Y.-C. Zhang, Y. Zhao and J. Gao, *Chem. Eng. J.*, 2024, **483**, 149253.
94 W. Zhang, Y. Lei, F. Ming, Q. Jiang, P. M. F. J. Costa and H. N. Alshareef, *Adv. Energy Mater.*, 2018, **8**, 1801840.
95 J. Coelho, R. F. Correia, S. Silvestre, T. Pinheiro, A. C. Marques, M. R. P. Correia, J. V. Pinto, E. Fortunato and R. Martins, *Microchim. Acta*, 2022, **190**, 40.
96 P. Yadav, A. Basu, A. Suryawanshi, O. Game and S. Ogale, *Adv. Mater. Interfaces*, 2016, **3**, 1600057.
97 Y. Gao, J. Zhang, X. Luo, Y. Wan, Z. Zhao, X. Han and Z. Xia, *Nano Energy*, 2020, **72**, 104666.
98 M. Yuan, F. Luo, Y. Rao, W. Ying, J. Yu, H. Li and X. Chen, *IEEE Electron Device Lett.*, 2022, **43**, 327–330.
99 A. Imbrogno, J. Islam, C. Santillo, R. Castaldo, L. Sygellou, C. Larrigy, R. Murray, E. Vaughan, M. K. Hoque, A. J. Quinn and D. Iacopino, *ACS Appl. Electron. Mater.*, 2022, **4**, 1541–1551.
100 A. Jrondi, G. Buvat, F. D. L. Pena, M. Marinova, M. Huvé, T. Brousse, P. Roussel and C. Lethien, *Adv. Energy Mater.*, 2023, **13**, 2203462.
101 F. Huang, S. Zhou, Z. Yan, S. Wang, H. Zhang, S. Wang and S. Zhou, *Appl. Surf. Sci.*, 2023, **619**, 156757.
102 Y. Zhao, L. Li, D. Zhou, Y. Ma, Y. Zhang, H. Yang, S. Fan, H. Tong, S. Li and W. Qu, *Angew. Chem., Int. Ed.*, 2024, **63**, e202404728.
103 X. Cao, C. Ma, L. Luo, L. Chen, H. Cheng, R. S. Orenstein and X. Zhang, *Adv. Fiber Mater.*, 2023, **5**, 1141–1197.
104 X. Li, P. Xu, Y. Tian, A. Fortini, S. H. Choi, J. Xu, X. Tan, X. Liu, G. Chen, C. Zhang, X. Lu, L. Jin, Q. Wang, L. Shen and Y. Lu, *Adv. Mater.*, 2022, **34**, 2107787.
105 F. Luo, T. Lyu, D. Wang and Z. Zheng, *Green Chem.*, 2023, **25**, 8950–8969.
106 M. D. Zhang, B. Chen and M. B. Wu, *Acta Phys.-Chim. Sin.*, 2022, **38**, 2101001.
107 P. Molaiyan, S. Bhattacharyya, G. S. dos Reis, R. Sliz, A. Paolella and U. Lassi, *Green Chem.*, 2024, **26**, 7508–7531.
108 M. Curcio, S. Brutti, L. Caripoti, A. De Bonis and R. Teghil, *Nanomaterials*, 2021, **11**, 3183.
109 N. A. Banek, D. T. Abele, K. R. McKenzie Jr. and M. J. Wagner, *ACS Sustainable Chem. Eng.*, 2018, **6**, 13199–13207.
110 C. Zhou, K. Zhang, M. Hong, Y. Yang, N. Hu, Y. Su, L. Zhang and Y. Zhang, *Chem. Eng. J.*, 2020, **385**, 123720.
111 H. Wang, H. Wang, Y. Wang, X. Su, C. Wang, M. Zhang, M. Jian, K. Xia, X. Liang, H. Lu, S. Li and Y. Zhang, *ACS Nano*, 2020, **14**, 3219–3226.
112 D. Yang, H. K. Nam, T.-S. D. Le, J. Yeo, Y. Lee, Y.-R. Kim, S.-W. Kim, H.-J. Choi, H. C. Shim, S. Ryu, S. Kwon and Y.-J. Kim, *ACS Nano*, 2024, **18**, 1237–1237.
113 P. Zhu, X. Xiong, D. Wang and Y. Li, *Adv. Energy Mater.*, 2023, **13**, 2300884.
114 E. Y. Choi, D. E. Kim, S. Y. Lee, C. B. Park and C. K. Kim, *Appl. Catal., B*, 2023, **325**, 122386.
115 M. Fan, J. Xu, Y. Wang, Q. Yuan, Y. Zhao, Z. Wang and J. Jiang, *Chem. – Eur. J.*, 2022, **28**, e202201996.
116 Y. Li, Y. Zhang, K. Qian and W. Huang, *ACS Catal.*, 2022, **12**, 1268–1287.
117 N. Wang, X. Bo and M. Zhou, *J. Colloid Interface Sci.*, 2021, **604**, 885–893.
118 A. Sinha and H. So, *Small Struct.*, 2023, **4**, 2300084.
119 Y. Wang, Y. Zhao, X. Li, L. Jiang and L. Qu, *Adv. Funct. Mater.*, 2022, **32**, 2203164.
120 H. Ling, R. Chen, Q. Huang, F. Shen, Y. Wang and X. Wang, *Green Chem.*, 2020, **22**, 3208–3215.
121 L. Meng, S. Chirtes, X. Liu, M. Eriksson and W. C. Mak, *Biosens. Bioelectron.*, 2022, **218**, 114742.
122 F. Mahmood, Y. Sun and C. Wan, *RSC Adv.*, 2021, **11**, 15410–15415.
123 H. Zhang, Y. Sun, Q. Li and C. Wan, *ACS Sustainable Chem. Eng.*, 2022, **10**, 11501–11511.
124 Q. Yang, L. Cao, S. Li, X. Zeng, W. Zhou and C. Zhang, *J. Anal. Appl. Pyrolysis*, 2023, **173**, 106074.
125 T.-S. D. Le, S. Park, J. An, P. S. Lee and Y.-J. Kim, *Adv. Funct. Mater.*, 2019, **29**, 1902771.
126 B. Kulyk, B. F. R. Silva, A. F. Carvalho, S. Silvestre, A. J. S. Fernandes, R. Martins, E. Fortunato and F. M. Costa, *ACS Appl. Mater. Interfaces*, 2021, **13**, 10210–10221.
127 J. Luo, Y. Yao, M. Niu, X. Duan, R. Wang and T. Liu, *ACS Omega*, 2019, **4**, 5870–5878.
128 L. Huang, L. Ling, J. Su, Y. Song, Z. Wang, B. Z. Tang, P. Westerhoff and R. Ye, *ACS Appl. Mater. Interfaces*, 2020, **12**, 51864–51872.
129 P. Zhao, G. Bhattacharya, S. J. Fishlock, J. G. M. Guy, A. Kumar, C. Tsonos, Z. Yu, S. Raj, J. A. McLaughlin, J. Luo and N. Soin, *Nano Energy*, 2020, **75**, 104958.
130 G. Daffan, A. Cohen, Y. Sharaby, R. Nudelman, S. Richter and F. Patolsky, *J. Energy Chem.*, 2024, **97**, 553–565.
131 T. Pinheiro, S. Silvestre, J. Coelho, A. C. Marques, R. Martins, M. G. F. Sales and E. Fortunato, *Adv. Mater. Interfaces*, 2021, **8**, 2101502.
132 S. Lee and S. Jeon, *ACS Sustainable Chem. Eng.*, 2019, **7**, 2270–2275.